4-24-2019 1:30 PM

Investigating the Rotary Mechanism of ATP Synthase Using Molecular Dynamics Simulations

Angela Marcela Murcia Rios
The University of Western Ontario

Supervisor
Konermann, Lars
The University of Western Ontario

Graduate Program in Chemistry
A thesis submitted in partial fulfillment of the requirements for the degree in Master of Science

Abstract

F_1-ATPase is a motor protein that can use ATP hydrolysis to drive rotation of the central γ subunit. The γ C-terminal helix constitutes of the rotor tip that is seated in an apical bearing formed by the $\alpha_3\beta_3$ head. It remains uncertain to what extent the γ conformation during rotation differs from that seen in rigid crystal structures. Existing models assume that the entire γ subunit participates in every rotation. Here we develop a molecular dynamics (MD) strategy to model the off-axis forces acting on γ in F_1-ATPase. MD runs showed stalling of the rotor tip and unfolding of the γ C-terminal helix. MD-predicted H-bond opening events coincided with experimental HDX patterns obtained in our laboratory. HDX-MS data suggests that *in vitro* operation of F_1-ATPase is associated with significant rotational resistance in the apical bearing. These conditions cause the γ C-terminal helix to get "stuck" while the remainder of γ continues to rotate. This scenario contrasts the traditional "greasy bearing" model that envisions smooth rotation of the γ C-terminal helix. Our work also demonstrates that MD simulations can provide insights into protein dynamic features that are invisible in static X-ray crystal structures.

Keywords

ATP Synthase, ATP Hydrolysis, Molecular Dynamics Simulation, Mass Spectrometry, Hydrogen Deuterium Exchange

Co-Authorship Statement

The work in Chapter 2 was published in the following article:

> Murcia Rios, A., Vahidi, S., Dunn S. D. & Konermann, K. (2018) Evidence for a Partially Stalled γ Rotor in F_1-ATPase from Hydrogen-Deuterium Exchange Experiments and Molecular Dynamics Simulations. *J. Am. Chem. Soc.* 140:14860. Reproduced with permission. Copyright © 2018, American Chemical Society.

The molecular dynamics simulation section in this manuscript was carried out and written by the author (A.M.R.). The author (A.M.R.) was responsible for developing the off-axis force rotation through the manipulation of GROMACS COM pulling code. Subsequent revisions to the manuscript were done by the author and Dr. Lars Konermann. All HDX-MS experiments were conducted by Dr. Siavash Vahidi.

Acknowledgments

I would like to express my sincerest appreciation to Dr. Lars Konermann for giving me this opportunity to participate in his wonderful research group since September of 2016. I would not know where I would be without his constant support and guidance during the exploration of this complex biomolecular system, which I have grown very fond of. It is because of his work and the work of Dr. Viktor N. Staroverov, that I have learned to appreciate the power of computer simulations.

I would also like to thank the rest of the Konermann research group especially Haidy, Ming, Victor, and Maryam, for dealing with me bragging about the awesome videos I make, as well as their support and feedback throughout my journey in this group. Courtney, Katja, Quentin, Vincent, Leanne, Insa, Nastaran, Elnaz, Drishti, Derek, Justin, Alex, Kwang, and the ones mentioned above have made my stay at the Konermann group unforgettable, and for that I owe them many thanks.

I also thank Dr. Stanley Dunn for sharing his wonderful knowledge about ATPase, and Dr. Siavash Vahidi for sharing his experimental work and insights with me. The work here would obviously not been possible without their feedback and expertise.

Lastly, I would like to thank Daniela, my parents, and my better half, Slava, for constantly showing me support and encouragement throughout my educational career. Without them and the support of my extended family and friends, I would not be where I am today. No words can express the immense love and gratitude I have towards them, and so, this work is dedicated to all of you.

Table of Contents

Abstract i

Co-Authorship Statement ii

Acknowledgments iii

Table of Contents iv

List of Symbols and Abbreviations vi

1 Introduction 1

1.1 Structure and Function of ATP Synthase ... 2

1.1.1 F_O Domain ... 2

1.1.2 F_1 Domain ... 4

1.2 Hydrogen-Deuterium Exchange Mass Spectrometry ... 8

1.2.1 HDX-MS Experiments for F_OF_1 ATP Synthase ... 8

1.2.2 HDX-MS Experiments for F_1 ATP Synthase ... 10

1.3 Molecular Dynamics Simulations ... 13

1.3.1 Integration of Newton's Second Law of Motion ... 13

1.3.2 Initial Conditions ... 15

1.3.3 Water Models ... 16

1.3.4 Force Fields ... 16

1.3.5 Energy Minimization ... 20

1.3.6 Thermostats and Barostats ... 20

1.3.7 Constraints ... 21

1.4 Steered Molecular Dynamics ... 21

1.4.1 Enforced Rotation ... 22

1.4.2 Center-of-Mass Pulling ... 22

1.5 Scope of the Thesis ... 25

References ... 27

2 Evidence for a Partially Stalled γ Rotor in F1-ATPase from H/D Exchange Experiments and Molecular Dynamics Simulations 30

2.1 Introduction 30
2.2 Methods 34
2.3 Results and Discussion 38
2.3.1 Enforced Bulk Rotation Simulations 38
2.3.2 Off-Axis Force Simulations 40
2.3.3 Behavior of the Apical Bearing 42
2.4 Conclusion 46
References 48

3 Conclusions and Future Work 52

3.1 Conclusions 52
3.2 Future Work – Off-Axis Force Rotation Studies of F_OF_1 53
References 55

Appendix I – Permissions 57

Curriculum Vitae 59

List of Symbols and Abbreviations

ADP — adenosine diphosphate

AMBER — assisted model building with energy refinement

AMP-PNP — adenosine 5′-(β,γ-imido)triphosphate

ATP — adenosine triphosphate

ATPase — ATP synthase

CHARMM — chemistry at Harvard molecular mechanics

COM — center of mass

Cryo-EM — cryogenic electron microscopy

E. coli — *Escherichia coli*

FCCP — carbonyl cyanide 4-(trifluoromethoxy)phenylhydrazone

FFT — Fast Fourier transform

GPU — graphics processing unit

HDX — hydrogen/deuterium-exchange

I_{ADP} — ADP inhibited state

$I_{AMP\text{-}PNP}$ — AMP-PNP inhibited state

$I_{MG\text{-}dep}$ — Mg^{2+}-depleted inhibited state

LINCS — linear constraint solver

MD — molecular dynamic

MS — mass spectrometry

MW — molecular weight

NMR — nuclear magnetic resonance

OPLS/AA — optimized potential for liquid Simulation - all atom

OSCP — oligomycin sensitivity conferral protein

PME — particle mesh Ewald

PBC — periodic boundary conditions

PDB — protein data bank

P_i — inorganic phosphate group

PMF — proton-motive force

SMD — steered molecular dynamic

SPC/E — extended simple point charge

TIP3P — transferable intermolecular potential with 3 points

TIP4P — transferable intermolecular potential with 4 points

TIP5P — transferable intermolecular potential with 5 points

W — working state

W_{FCCP} — FCCP working state

W_{PMF} — proton-motive force working state

1 Introduction

The ATP synthase family of enzymes represents the world's smallest enzymatic motors. These proteins are capable of synthesizing and hydrolyzing adenosine triphosphate (ATP) the "energy currency of the cell". ATP synthase generates ATP from adenosine diphosphate (ADP) and inorganic phosphate (P_i) during cellular respiration through the use of a proton-motive force (PMF). This PMF is an electrochemical gradient of protons across the mitochondrial membrane in eukaryotes, or the plasma membrane in bacteria. Similarly, in chloroplasts, ATP is synthesized during photosynthesis using a PMF that is created across the thylakoid membrane. Depending on the physiological conditions, ATP synthases can also be required to operate in reverse, i.e., in the ATP hydrolysis direction. For example, under anerobic conditions where the respiratory chain is inactive, bacterial ATP synthases can hydrolyze ATP that has been synthesized by glycolysis.[1] This process is essential for maintaining PMF which is required for numerous essential functions in every living cell. ATP hydrolysis in mitochondria, chloroplasts and some bacteria is normally inhibited, but it can be artificially activated *in vitro*. Throughout this work, we will focus on bovine mitochondrial as well as *E. coli* ATP synthase, due to the availability of high resolution crystallographic data for these systems.[2-5] In addition, our own laboratory has generated detailed experimental data on *E. coli* ATP synthase.[6,7] By properly understanding the mechanism of ATP synthase, we may be able to improve antibiotic targeting for organisms such as *Mycobacterium tuberculosis*[8,9] and other pathogenic bacteria.

1.1 Structure and Function of ATP Synthase

ATP synthases from mitochondria and bacteria differ in their amino acid sequence, although their structures share a high degree of similarity.[1] Both systems are composed of two rotary motors, F_O and F_1, which are mechanically joined by central and peripheral stalks (Figure 1.1).[10,11] When separated, these two motors rotate in opposite directions. The F_O membrane-bound domain is driven by PMF, while the soluble F_1 domain is driven by ATP hydrolysis. These rotary motors are composed of multiple subunits. Their structure and function will be further discussed in the sections below.

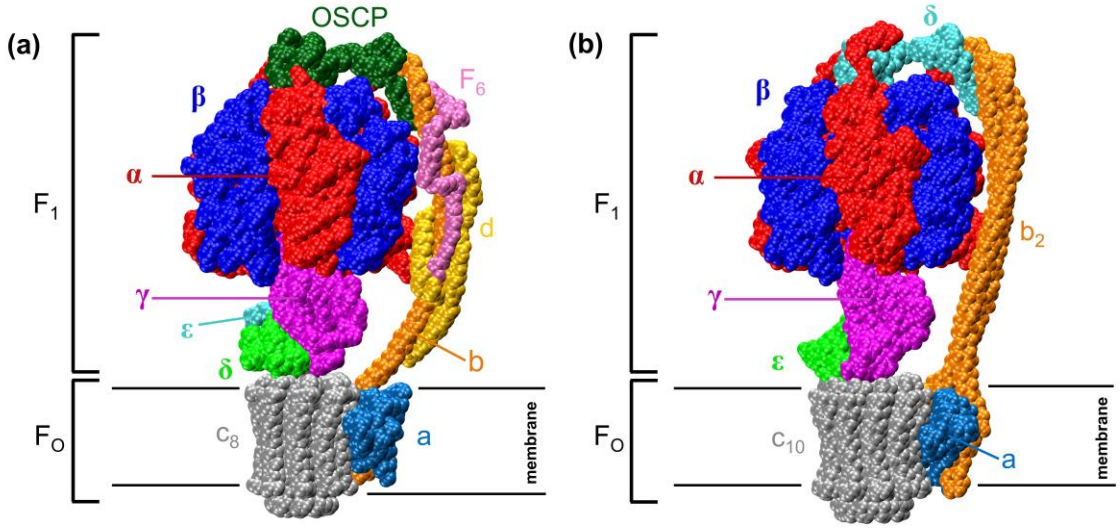

Figure 1.1 Structure of ATP Synthase.
Cryo-electron microscopy structures of (a) mitochondrial ATPase (PDB code 5ARA) (b) bacterial (*E. coli*) ATPase (PDB code 5T4P). VMD visualization program was used to generate this figure.

1.1.1 F_O Domain

The membrane embedded F_O domain (Figure 1.1) is made up of the c_n ring (c_8 in bovine mitochondria, c_{10} in *E. coli*), the *a* subunit, and the peripheral stalk, along with some smaller subunits in mitochondrial ATP synthase (not shown in Figure 1.1 for simplicity). The peripheral stalk is composed of the δ, and 2 *b* subunits in *E. coli* and OSCP, *b*, *d*, and

F$_6$ in bovine mitochondria. The peripheral stalk connects the *a* subunit to the $\alpha_3\beta_3$ head of the F_1 domain to form the non-rotating "stator" of the enzyme. The c_n ring connects to the central stalk of F_1 that comprises γ and forms the "rotor" of the system. The c_n ring moves by using electrochemical energy stored in the PMF. Protons are translocated via the a/c_n ring front interface (Figure 1.2b) by spontaneously neutralizing a negatively charged carboxyl group found on either an aspartate residue (Asp61 in *E. coli*) or glutamate (Glu58 in in bovine) in the c_n ring.[10] The neutralized residues favour a more hydrophobic environment, forcing them to move into the hydrophobic membrane layer.[10,12] On the back of the a/c_n ring interface, conditions favour the deprotonation of the carboxyl group, allowing the proton to be discharged on the other side (low $[H^+]$) of the membrane.[12] These protonation/deprotonation events force the c_n ring to rotate as shown in Figure 1.2b. This rotation is coupled to the motion of the central stalk of the F_1 domain which triggers ATP synthesis.

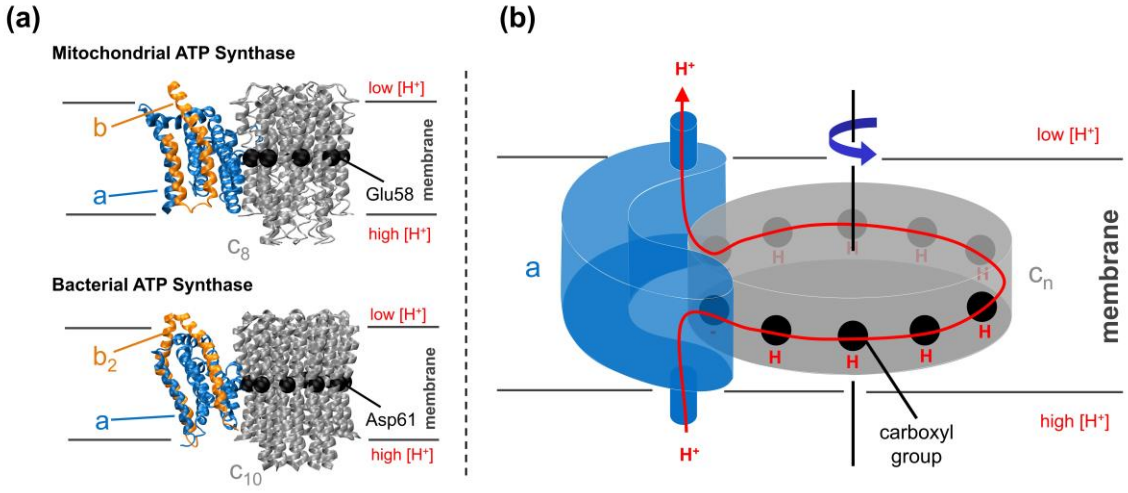

Figure 1.2 Structure and schematic diagram of membrane intrinsic subunits.
(a) mitochondrial (PDB code 5ARA) and bacterial (PDB code 5T4P) c_n ring (grey), *a* subunit (blue), membrane-intrinsic *b* and b_2 subunit sections (orange), and carbonyl containing residues (black). (b) schematic diagram of proton translocation from high concentration to low concentration between the membrane.

1.1.2 F_1 Domain

The soluble F_1 domain is the catalytic portion of the complex that synthesizes or hydrolyzes ATP.[1] It is composed of the γ subunit, which rests approximately in the center of the $\alpha_3\beta_3$ head (Figure 1.3).[10,11] Attached to the γ subunit is the ε subunit in *E. coli*, or the ε and δ subunits in the mitochondrial F_1 domain. These subunits, along with γ, make up the central stalk.[2] *E. coli* crystal structures[5] all show the ε subunit in its autoinhibited conformation (Figure 1.3b), which prevents rotation of γ under physiological conditions. For comparison, the bovine crystal structures[3] show the ε equivalent subunit (δ subunit) in its non-inhibited conformation (Figure 1.3a).

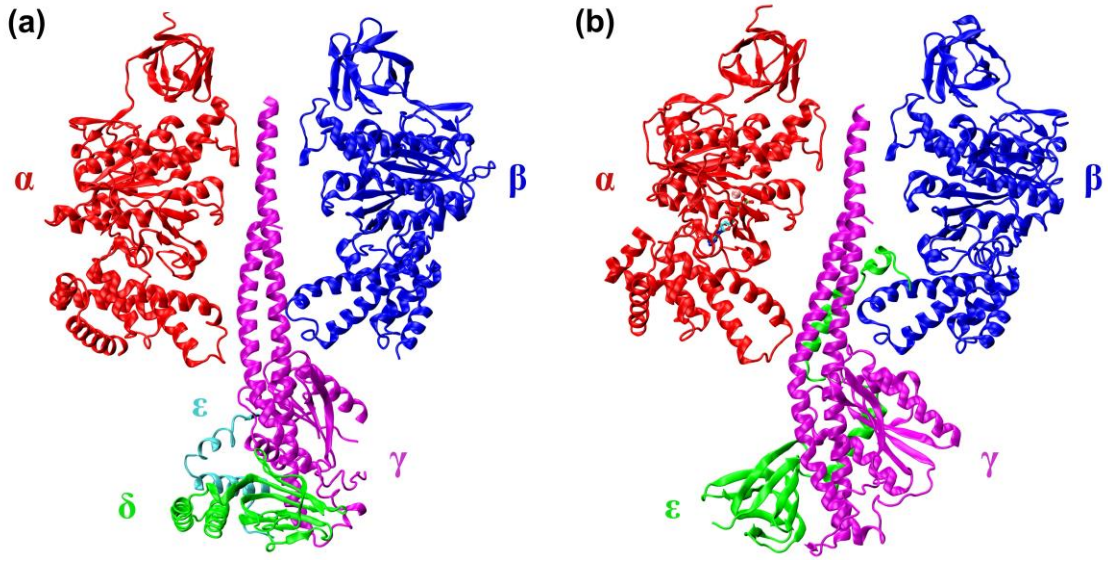

Figure 1.3 Structure of F_1-ATP Synthase.
(a) F_1-ATPase crystal structure of mitochondrial bovine (PDB code 1E79), showing only one αβ pair, γ subunit (magenta), ε subunit (cyan), and δ subunit (green). (b) F_1-ATPase crystal structure of *E. coli* (PDB code 3OAA), showing one αβ pair, γ subunit (magenta), and inhibited conformation of ε subunit (green).

Under normal physiological conditions, ATP is synthesized by the rotation of the central stalk/c_n ring, which is powered by the PMF. When the F_1 domain is isolated biochemically, it retains the capability to catalyze the rotation of the central stalk via ATP hydrolysis.[13] The isolated F_1 domain is usually referred to as F_1-ATPase. To understand how F_1-ATPase works, the structure of the F_1 domain needs to be looked at in further detail.

F_1 consists of three alternating pairs of α and β subunits, resembling the segments of an orange, which surround the central γ subunit (Figure 1.4a).[3] Each α and β subunit are in different conformational states; α_{TP}/β_{TP}, α_{DP}/β_{DP}, or α_E/β_E.[1] "TP" refers to the ATP bound form, "DP" represents the ADP-bound conformation, and "E" stands for empty, representing different stages of the catalytic cycle (Figure 1.4b). In most crystal structures AMP-PNP (a non-hydrolysable ATP analog) is bound to β_{TP}, rather than ATP. ADP is bound to β_{DP}, while β_E ("empty") has no associated nucleotide. β_{TP} and β_{DP} have a more closed structure compared to β_E. The latter has a distinctively open conformation.[13] The three β subunits contain the active sites that are involved in ATP/ADP interconversion. In addition, each of the three α subunits has one nucleotide permanently bound in a non-catalytic site.

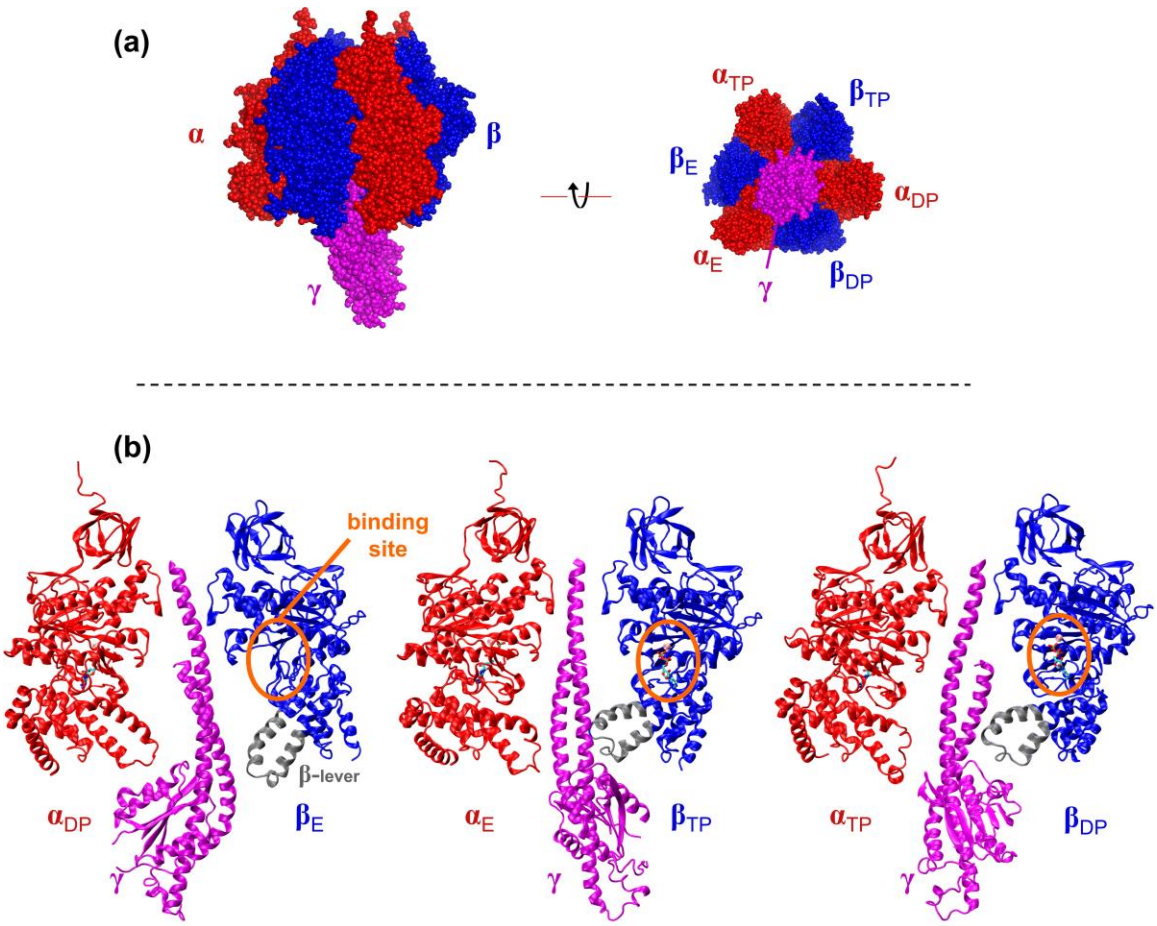

Figure 1.4 α and β subunit conformations with respects to the γ subunit.
(a) F_1 domain of bovine mitochondria (PDB code 1E79), showing the α (red), β (blue), γ (magenta), and omitting ε and δ subunits. (b) Each frame shows the different conformational states of α and β subunits depicted in panel (a).

From the observations of the different conformational states of the α and β subunits, it is believed that the asymmetric γ subunit must rotate as the result of mechanical forces induced by conformational changes in the $\alpha_3\beta_3$ head.[13] Through biochemical experiments,[12,14-17] the mechanism of the central stalk rotation became apparent, and a proposed cycle of ATP hydrolysis was determined.[18] According to this mechanism, the central stalk turns counter clockwise during ATP hydrolysis (when viewed from the F_O side), where the γ subunit rotates due to each β subunit cycling through the three conformational states (Figure 1.4 and Figure 1.5).[12,14,15] As ATP binds to β_E, it causes a

conformational change from β_E to β_{TP}, which then drives partial rotation of the central stalk. From here, ATP gets broken down to ADP and P_i, which triggers further central stalk rotation along with a conformational change from β_{TP} to β_{DP}. ADP and P_i are then released, changing the β subunit back to the β_E conformation. Taken together, the aforementioned conformational changes cause the β-levers to turn the γ subunit by 120°, such that three ATP hydrolysis events are required for one complete rotation (Figure 1.5).[12,14,15] Further experiments revealed that each 120° step can be broken down into two substeps of approximately 40° and 80°.[17]

As of now, there is limited understanding of the exact conformational changes experienced by the γ subunit during hydrolysis. Therefore, the challenge remains to properly model the γ subunit rotation and to understand the mechanochemical coupling between rotation and catalytic events in the $\alpha_3\beta_3$ head.

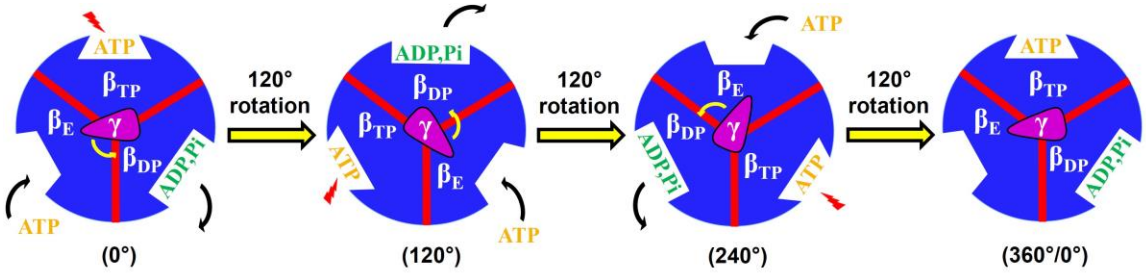

Figure 1.5 Schematic diagram of ATP hydrolysis cycle.
Changes in β subunit conformations due to nucleotide binding hydrolysis and release (red and black arrows) triggers 120° rotations of the γ subunit (yellow arrow).

1.2 Hydrogen-Deuterium Exchange Mass Spectrometry

Hydrogen deuterium exchange (HDX) mass spectrometry (MS) is a technique used to interrogate protein structure and dynamics in solution.[19] HDX-MS monitors the deuteration of backbone amide NH sites when the protein is exposed to D_2O. Each of these deuteration events increases the protein mass by 1 Da, such that HDX kinetics can be probed by monitoring the mass increase of specific protein segments (peptides) as a function of time. HDX rates are modulated by the stability of NH···OC backbone H-bonds that mediate the formation of secondary structure (α helices or β-sheets). Protein regions that are tightly folded with very stable H-bonds exhibit slow HDX. Conversely, regions that are flexible and undergo frequent H-bond opening/closing events will undergo rapid HDX. Dr. Siavash Vahidi in our laboratory performed the first *in situ* HDX-MS experiments of catalytically active *E. coli* F_1- and F_OF_1-ATPase.[6,7] The following sections provide an overview of these experimental results, which provide the foundation and motivation for the MD simulations of the current thesis.

1.2.1 HDX-MS Experiments for F_OF_1 ATP Synthase

In an initial set of experiments, HDX-MS was applied to intact *E. coli* F_OF_1-ATPase embedded in bacterial membrane vesicles under three different experimental conditions: ADP-inhibited F_OF_1 (I_{ADP}), proton pumping F_OF_1 against a PMF-mediated counter-torque (W_{PMF}), and proton pumping F_OF_1 with an uncoupler (FCCP) that prevents PMF buildup (W_{FCCP}). For both the W_{PMF} and W_{FCCP} systems, an ATP regeneration system was used to ensure an adequate supply of ATP for maintaining rotation during an extended period (~45 min).

The key finding of these experiments was that under W_{PMF} conditions, γ experienced major destabilization at the C-terminus, in the apical bearing region of the $\alpha_3\beta_3$ head. This destabilization was evident from greatly enhanced HDX levels in the corresponding region as seen when comparing I_{ADP} (green in Figure 1.6b) to W_{PMF} (red in Figure 1.6c). It was proposed that this distortion could be due to resistive or "frictional" forces encountered in the tight bearing region of the $\alpha_3\beta_3$ head (Figure 1.6a).[7] Under normal physiological conditions, F_OF_1 operates in the presence of PMF, therefore it is likely that this distortion is part of the regular F_OF_1 operation. These findings were consistent with computational data by Okazaki and Hummer that also suggested frictional forces near the apical bearing when γ is rotated with an applied torque.[20]

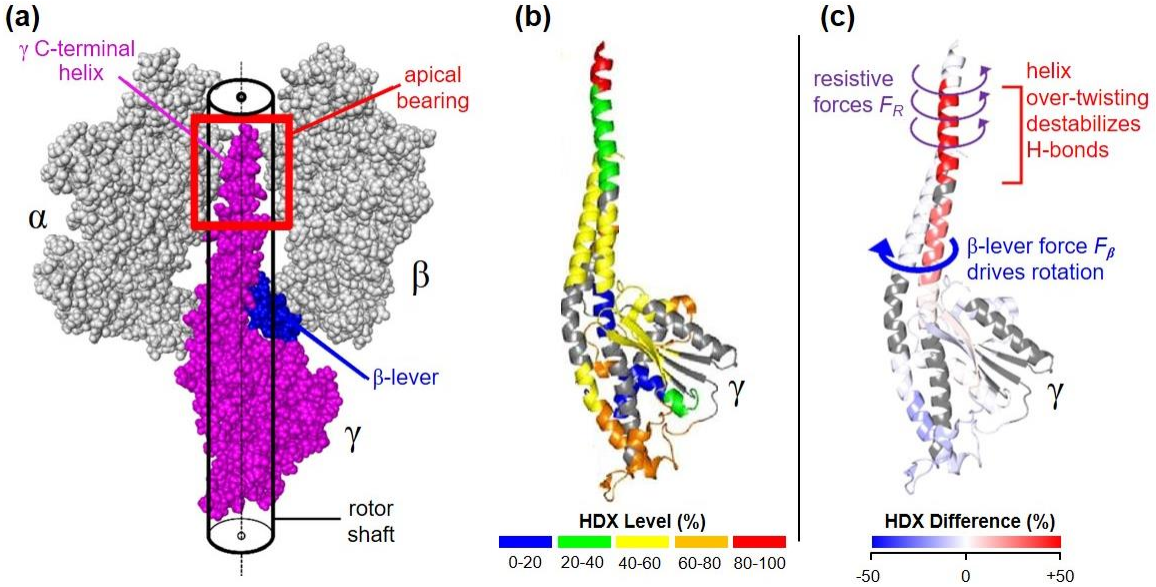

Figure 1.6 Schematic and HDX difference map of γ subunit in F_OF_1 ATP synthase. (a) Schematic of an αβ pair along with the γ subunit, and its labeled regions. (b) HDX levels of I_{ADP} γ for an HDX period of 45 min. (c) Deuteration difference map of γ W_{PMF} vs. I_{ADP}. Dark red coloring highlights enhanced deuteration (i.e. distortion of γ C-terminal helix) due to resistive forces in apical bearing region. (reproduced from Vahidi *et al.*[7])

1.2.2 HDX-MS Experiments for F_1 ATP Synthase[1]

Isolated F_1-ATPase represents a much more tractable system compared to F_OF_1. This sub-complex is freely soluble in solution such that the measurements can be conducted in the absence of membrane vesicles, thereby facilitating the experimental workflow. F_1-ATPase retains the ability to drive γ rotation via ATP hydrolysis.[15,21-26] Due to the lack of a c_{10} ring, the "foot" of γ protrudes into the solvent. Because of its reduced size, F_1-ATPase is well suited for exploring the conformational dynamics of the γ rotor and the role of $\gamma\cdots\alpha_3\beta_3$ contacts in the apical bearing. It has traditionally been envisioned that hydrophobic residues lining the inside of the apical bearing allow smooth rotation of the γ C-terminal helix (together with the rest of γ).[3] Interestingly, Hilbers *et al.*[27] recently demonstrated that γ rotation in F_1-ATPase still takes place after disulfide linking the γ C-terminal helix with $\alpha_3\beta_3$. Thus, it appears that F_1-ATPase can function with a stalled ("stuck") apical rotor tip, via local unfolding of the γ C-terminal helix, and with swivel rotation around ϕ/ψ angles.[27] The implications of those findings[27] for unmodified F_1-ATPase are unclear. For example, it seems possible that even under regular physiological conditions the γ C-terminal helix may continue to be stalled in the apical bearing. In other words, it remains to be established if all parts of γ participate in rotation under normal operating conditions.

To determine whether all of γ plays a roll in rotation, HDX-MS experiments were conducted in our laboratory. Three non-rotating states were examined to distinguish trivial substrate binding effects from features that are uniquely linked to rotation. (i) The

---

[1] Reproduced in part from **Murcia Rios, A.**, Vahidi, S., Dunn S. D. & Konermann, K. (2018) Evidence for a Partially Stalled γ Rotor in F_1-ATPase from Hydrogen-Deuterium Exchange Experiments and Molecular Dynamics Simulations. *J. Am. Chem. Soc.* 140:14860. Copyright © 2018, American Chemical Society.

ADP-inhibited state I_{ADP} has Mg·ADP and azide permanently bound in at least one catalytic site.[24,28] (ii) $I_{AMP\text{-}PNP}$ represents a state where the enzyme binds azide and the non-hydrolyzable substrate analog AMP-PNP.[28] (iii) The Mg^{2+}-depleted state $I_{Mg\text{-}dep}$ represents F_1-ATPase that is essentially nucleotide-free because its nucleotide binding affinity is reduced by orders of magnitude.[29] (iv) In addition to these three inactive states the working state *W* was characterized where F_1-ATPase underwent ATP hydrolysis-driven γ rotation.

HDX-MS revealed significant destabilization of H-bonds in the γ C-terminal helix during rotational catalysis. For the inactive states I_{ADP} and $I_{Mg\text{-}dep}$, this region showed moderate deuteration. In contrast, γ rotation under *W* conditions caused significantly enhanced HDX levels, indicating a marked destabilization of the γ C-terminal helix (Figure 1.7). Similar to the scenarios discussed above for F_OF_1, this effect suggests "friction-like" interactions between the γ C-terminal helix and $\alpha_3\beta_3$. More specifically, while the β-levers force γ to turn, the γ C-terminal helix experiences rotational resistance in the apical bearing. This resistance causes helix over-twisting. A detailed analysis of the deuteration patterns revealed the existence of both EX2 and EX1 behavior. EX2 deuteration indicates very rapid H-bond opening/closing events, taking place on time scales much faster than 0.1 s. EX1 signifies very slow conformational fluctuations on time scales >> 0.1 s.[19] One possible interpretation of these experimental data is that the rotor tip undergoes enhanced thermal fluctuations during rotation (EX2), in addition to occasional stalling with local unfolding (EX1).[6]

The aforementioned interpretation of HDX data in terms of rotational resistance ("friction") in F_1-ATPase is reminiscent of the F_OF_1 data that were discussed in section 1.2.1.[7] However, one has to reconcile this proposed F_1-ATPase scenario with the fact that γ destabilization in F_OF_1 takes place only in the presence of PMF,[7] while for F_1-ATPase this phenomenon occurs without an energized membrane. From the results of this thesis it will be seen that the surprising vulnerability of the γ C-terminal helix in F_1-ATPase reflects the absence of a membrane-anchored c_{10} ring that stabilizes the rotation axis in the case of intact F_OF_1. The data discussed below will demonstrate that all the available data supports the proposed scenario, where $\gamma\cdots\alpha_3\beta_3$ contacts in the apical bearing of F_1-ATPase favor occasional stalling and unfolding of the apical rotor tip during catalytic turnover.

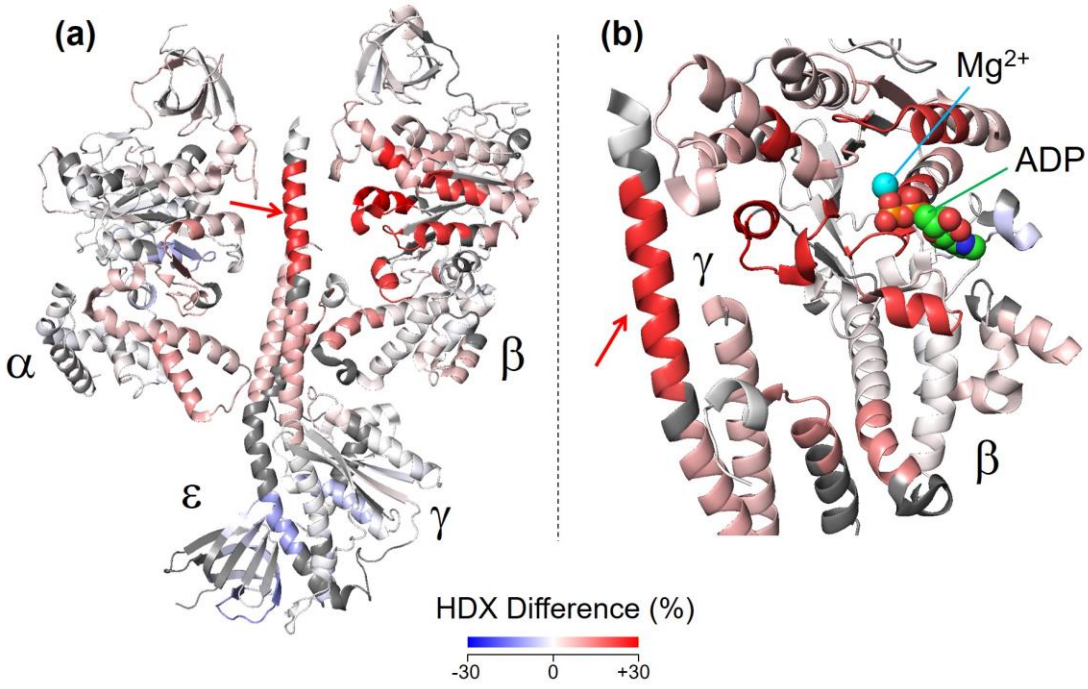

Figure 1.7 HDX difference map of αβ pair and γ subunit in F_1 ATP synthase.
(a) HDX difference map of *W*. (b) Close-up view of the β catalytic site in *W*. Red arrows highlight the region where the γ C-terminal helix gets destabilized during rotation under *W* conditions. Reproduced with permission. Copyright © 2018, American Chemical Society.

1.3 Molecular Dynamics Simulations

Molecular dynamics (MD) simulations are a powerful tool that can complement experimental results by providing atomistic insights into time-dependent changes in (bio)molecular systems.[30] The development of MD simulation techniques would not have been possible without the innovative minds of Karplus, Levitt and Warshel, who won the 2013 Nobel Prize in Chemistry for combining classical and quantum mechanical methods for the "development of multiscale models of complex chemical systems". Over the past few years, MD simulations have played an important role in efforts to decipher the F_OF_1 rotary mechanisms.[18,20,21,31-35] Yet, we still do not fully understand, at the molecular level, how the F_OF_1 (or F_1) conformational changes are coupled to rotation of γ.

1.3.1 Integration of Newton's Second Law of Motion

MD simulations use the classical equations of motion from Newtonian mechanics, together with molecular mechanics force fields, to predict the time-dependent motion of molecular systems.[36] Newton's second law of motion states that the position of a particle $\boldsymbol{r}_i$, with mass m_i and acceleration a_i, can be described in space as time evolves (equation 1.1). It can relate the force $\boldsymbol{F}_i$, or derivative of the potential energy U, to the changes in position as a function of time.

$$\boldsymbol{F}_i = m_i \boldsymbol{a}_i = m_i \frac{d^2 \boldsymbol{r}_i}{dt^2} = -\frac{\partial U(\boldsymbol{r}_i, \ldots, \boldsymbol{r}_N)}{\partial \boldsymbol{r}_i} \qquad (1.1)$$

For multi-atom systems, equation 1.1 cannot be solved analytically due to its complexity. Therefore, numerical algorithms have been developed. Some of these strategies include the Leap-frog[37], Verlet[38], or velocity Verlet[39] algorithms all of which assume that positions, velocities, and accelerations can be approximated by a Taylor

series expansion (equation 1.2 and equation 1.3). These algorithms revolve around the time increment δt which is used to calculate the next set of positions $\boldsymbol{r}$ and velocities $\boldsymbol{v}$. This number is usually in the order of 1 fs (see section 1.3.7 Constraints).

$$\boldsymbol{r}(t+\delta t) = \boldsymbol{r}(t) + \boldsymbol{v}(t)\delta t + \frac{1}{2}\boldsymbol{a}(t)\delta t^2 + \frac{1}{6}\frac{d^3\boldsymbol{r}(t)}{dt^3}\delta t^3 + \cdots \tag{1.2}$$

$$\boldsymbol{v}(t+\delta t) = \boldsymbol{v}(t) + \boldsymbol{a}(t)\delta t + \frac{1}{2}\frac{d^2\boldsymbol{v}(t)}{dt^2}\delta t^2 + \frac{1}{6}\frac{d^3\boldsymbol{v}(t)}{dt^3}\delta t^3 + \cdots \tag{1.3}$$

The leap-frog algorithm calculates the velocities first at time $t + \frac{1}{2\delta t}$, which are then used to calculate the positions and velocities at time $t + \delta t$ by using equation 1.4 and equation 1.5.

$$\boldsymbol{r}(t+\delta t) = \boldsymbol{r}(t) + \boldsymbol{v}\left(t + \frac{1}{2}\delta t\right)\delta t \tag{1.4}$$

$$\boldsymbol{v}\left(t + \frac{1}{2}\delta t\right) = \boldsymbol{v}\left(t - \frac{1}{2}\delta t\right) + \boldsymbol{a}(t)\delta t \tag{1.5}$$

The Verlet algorithm, on the other hand, is based on the Taylor expansion of $r(t+\delta t)$ and $r(t-\delta t)$, which results in equation 1.6. This algorithm does not involve explicit velocities and therefore it is rarely used.

$$\boldsymbol{r}(t+\delta t) = 2\boldsymbol{r}(t) - \boldsymbol{r}(t-\delta t) + \boldsymbol{a}(t)\delta t^2 + \cdots \tag{1.6}$$

The velocity Verlet overcomes the aforementioned obstacle and is more commonly used (equation 1.7 and equation 1.8).

$$\boldsymbol{r}(t+\delta t) = \boldsymbol{r}(t) + \boldsymbol{v}(t)\delta t + \frac{1}{2}\boldsymbol{a}(t)\delta t^2 + \cdots \tag{1.7}$$

$$\boldsymbol{v}(t+\delta t) = \boldsymbol{v}(t) + \frac{1}{2}\big(\boldsymbol{a}(t) + \boldsymbol{a}(t+\delta t)\big)\delta t + \cdots \tag{1.8}$$

To initiate these algorithms, the program must have starting positions and velocities in order to calculate the next set of positions and velocities to form a simulation run.

1.3.2 Initial Conditions

A protein simulation is typically started by choosing published X-ray crystal or nuclear magnetic resonance (NMR) coordinates that provide heavy atom starting coordinates. Missing hydrogen atoms are then inserted using an MD simulation software protocol (PDB2GMX in GROMACS).[40] For MD simulations in solution a box size needs to be defined such that periodic boundary conditions (PBCs) can be implemented. PBCs are used to avoid any surface artifacts with the solvent of choice by surrounding the system with copies of itself in all directions. Therefore, if a molecule were to leave from one side of the simulation box, it would re-enter the cell on the opposite side. This method models a continuous solution phase. To minimize the number of solvent molecules in the simulation, different box shapes can be used (i.e. cubic, rhombic dodecahedron, etc.) according to the geometry of the protein. The box containing protein is then filled with water using the appropriate water model (section 1.3.3).[41] A certain salt concentration can also be added by replacing random water molecules with the specific salt cations and anions (usually Na^+ and Cl^-, at a concentration of 150 mM).

Initial atomic velocities can be randomly assigned with a given absolute temperature T from a Maxwell-Boltzmann distribution (equation 1.9).

$$p(v_i) = \sqrt{\frac{m_i}{2\pi k_B T}} exp\left(-\frac{m_i v_i^2}{2kT}\right) \tag{1.9}$$

Where $p(v_i)$ is the probability distribution of atoms having initial velocities v_i, between v_i and $v_i + dv_i$, k_B is the Boltzmann constant and m is the mass of the atom.

1.3.3 Water Models

To properly simulate biomacromolecules, a proper aqueous environment needs to be met. This usually implies the use of water as the solvent for these systems. In most cases, water is modeled explicitly as discrete particles in the system rather than using an implicit model (modeled by a continuous dielectric medium).[42] Various types of water models exist in MD. They can be classified based in the number of simulated interactions sites, flexibility of covalent bonds, and polarizability.

The TIP3P[43] and SPC/E[44] water models are rigid three-site models that represent the H and O atoms as point charges. These models are most commonly used in large systems because of their low computational costs. They perform well in bulk solution, yet their surface tension properties are poor compared to experimental measurements.[45] To overcome this, the four-site TIP4P[46] and TIP4P/2005[47] water models have been developed. These models place the O charge on a massless virtual point that sits on the bisector of the HOH angle. The O charge can also be split between two virtual sites representing the lone pairs of electrons. These sites have a tetrahedral geometry and can be seen in models such as TIP5P.[48] Selection of a proper model can determine the quality of the simulation. However, no model can perfectly reproduce all properties of water.

1.3.4 Force Fields

Molecular mechanics (MM) force fields are used to calculate the potential energy of the system as a function of all atomic coordinates **r**, as required for integration of Newton's second law of motion (equation 1.1). Some of the most commonly used force fields are: Optimized Potential for Liquid Simulations – All Atom (OPLS/AA)[49] force field, which

is parameterized to fit experimental properties of liquids; The Chemistry at Harvard Molecular Mechanics (CHARMM)[50] and Assisted Model Building with Energy Refinement (AMBER)[51] force fields, which derive their charge parameters from density functional theory calculations and are intended to be used for proteins/macromolecules.

In general, MM models assume all atoms to be spheres (point charges) and bonds to be springs to make calculations simpler. The force fields contain equations with specific parameters that describe the interactions between the atoms and the state of the system. In general, these potential energies are calculated as given in equation 1.10.

$$U_{total} = U_{bonded} + U_{non-bonded} \tag{1.10}$$

Here, U_{bonded} are the potential energies associated with bonding types such as bond stretching, angle bending, or torsions. Each of these bonding types are associated with their own potential energy equations and parameters (equation 1.11).

$$U_{Bonded} = \sum_{bonds} \frac{1}{2} k_b (b - b_0)^2 + \sum_{angles} \frac{1}{2} k_\theta (\theta - \theta_0)^2 + \sum_{dihedrals} \frac{1}{2} k_\phi [1 + \cos(n\phi - \delta)] \tag{1.11}$$

The first term describes bond stretching (2-body term) where k_b is the force constant of the bond, b is the current bond length, and b_0 is the equilibrium bond length. The second term describes angle bending (3-body term) where k_θ is the force constant of the angle, θ is the distorted angle, and θ_0 is the equilibrium value. The last term describes torsion or dihedral angles (4-body term), where k_ϕ is the force constant of the dihedral angle, n is the multiplicity of the function, ϕ is the dihedral angle and δ is the phase shift. Other terms similarly exist that can be added to U_{bonded}. For simplicity, these other terms will not be mentioned here.

$U_{non-bonded}$ includes potential energies from van der Waals and electrostatic interactions, which are described by equation 1.12 and equation 1.13. Here, van der Waals interactions group all interactions that are not covalent or electrostatic such as London dispersion forces (dipole to induced dipole), Debye forces (permanent dipole to induced dipole), or Keesom forces (permanent dipole to permanent dipole). These interactions between a pair of atoms i and j are most commonly modeled using a Lennard-Jones potential (equation 1.12).[41]

$$U_{van\ der\ Waals} = 4\epsilon_{ij}\left[\left(\frac{\sigma_{ij}}{r_{ij}}\right)^{12} - \left(\frac{\sigma_{ij}}{r_{ij}}\right)^{6}\right] \tag{1.12}$$

Where ϵ and σ are parameters that define the position and depth of the minimum in the potential, and r_{ij} is the distance separating particles i and j. The r^{-6} term represents the attractive forces between atoms i and j averaging the Keesom, Debye, and London dispersion forces. The r^{-12} term represents the repulsion of the two atoms, and accounts for the Pauli exclusion principle. During simulations, the r^{-6} term in equation 1.12 becomes irrelevant for large values of r. Thus, a cutoff value can be introduced to treat these Lennard-Jones interactions.

The electrostatic non-bonding term is modelled by the Coulomb potential (equation 1.13), where q_i and q_j are the charges of the particles i and j, ε_0 is the vacuum permittivity, ε_r is the relative dielectric constant, and r_{ij} is the distance between the particles.

$$U_{Electrostatic} = \frac{1}{4\pi\varepsilon_0}\frac{q_i q_j}{\varepsilon_r r_{ij}} \tag{1.13}$$

A cutoff to the Coulomb potential can also be introduced, but the long-range nature of electrostatic interactions causes them to decrease slowly with increasing distance. Simple cutoffs therefore tend to induce electrostatic artifacts, especially when using PBC. This can be overcome by using Ewald summation[52] where the summation of equation 1.13 over all atom pairs can be split into two series (equation 1.14).[42]

$$\frac{1}{r_{ij}} = \frac{\mathrm{erfc}(\beta r)}{r_{ij}} + \frac{\mathrm{erf}(\beta r)}{r_{ij}} \tag{1.14}$$

Where $\mathrm{erf}(\beta r)$ is the error function, $\mathrm{erfc}(\beta r)$ is the complementary error function where $\mathrm{erfc}(\beta r) = 1 - \mathrm{erf}(\beta r)$, and β is the width of the Gaussian distributions. The first term of equation 1.14 is short-ranged meaning it will be negligible after a certain cutoff distance. The second term is long-ranged and is handled in the reciprocal space using Fourier transforms.[42] The last term usually scales to $O(N^2)$, which means as the system size increases the efficiency decreases. Particle Mesh Ewald (PME) summation[53,54] is able to accelerate the long-ranged term to $O(NlogN)$ by computing the reciprocal part on a mesh through the use of Fast Fourier transforms (FFT).

The use of cutoff schemes requires the computation of the distance between every pair of atoms to determine if they are within or beyond the cutoff for calculating non-bonded energies. The most efficient way is to use a Verlet neighbor search.[38] The Verlet scheme sorts all potential atom partners that lie within the cutoff distance and stores them in a list. Only atoms in this list are included for calculating forces at each integration step. As the particles change their positions, the algorithm updates the neighbor list in an efficient way.

1.3.5 Energy Minimization

The addition of hydrogen atoms and solvent molecules to the initial crystal structure often leads to clashes. Therefore, an energy minimization procedure must be applied to allow the system to relax so the possibility of destroying the initial conformation by "blowing up" the system is avoided.[41] One method that is commonly used is that of steepest decent (equation 1.15), where r_n is a vector containing all particle positions at step n, K_n is a small scalar distance increment, and ∇U is the gradient of the potential function. Here, the potential energy of the system is minimized until the maximum force within the system drops below a certain threshold, or until the number of force evaluations that have been performed reaches a user-specified number.

$$\boldsymbol{r}_{n+1} = \boldsymbol{r}_n - K_n \nabla U(\boldsymbol{r}_n) \tag{1.15}$$

1.3.6 Thermostats and Barostats

The system needs to be equilibrated either by bringing it to a predefined constant temperature using a thermostat, and/or by bringing it to a predefined pressure using a barostat. These methods are useful for keeping the system in a specific type of ensemble such as in a microcanonical (N,V,E), canonical (N,V,T), or isothermal–isobaric (N,P,T) ensemble. Some examples of commonly used thermostats are the weak-coupling scheme of Berendsen[55], stochastic randomization through the Andersen[56] thermostat, the extended ensemble Nosé-Hoover[57,58] scheme, and the modified Berendsen velocity-rescale thermostat.[59] The Berendsen and, better yet, the velocity-rescale methods are most useful for relaxing a system to a target temperature. To keep the system at a target ensemble, it is more common to use the Nosé-Hoover scheme. The most common

barostat algorithms are the Berendsen[55] algorithm that scales coordinates and box vectors every step, and the extended-ensemble Parrinello-Rahman[60] approach. One major step-back of the Berendsen barostat is that it does not give the exact NPT ensemble. Therefore, the Parrinello-Rahman method is mostly used.

1.3.7 Constraints

To help speed up simulation runs, the integration time step (δt) can be increased (to an order of 1 fs) by constraining bonds to eliminate fast vibrational bond motions. Commonly used constraining algorithms include SHAKE[61], SETTLE[62], and LINCS (linear constraint solver).[63] These algorithms use Lagrange multipliers to modify the forces on constrained bonds. The SHAKE algorithm solves the Lagrange multipliers to fulfill the constraint equations. This requires a relative tolerance where the program will iterate until the constraint equations are solved within the given tolerance. The SETTLE algorithm is an analytical solution to SHAKE, which is used when rigid water molecules are used in the simulations. LINCS is a two step non-integrative method. It resets bonds to their correct lengths after an unconstrained update. This method is much more stable and faster than the SHAKE algorithm.

1.4 Steered Molecular Dynamics

Due to computational costs, it can be challenging to model the conformational dynamics of proteins on physiological time scales.[41] Today, we are able to model thousands of protein atoms and their surrounding solvent for several milliseconds.[64] However, simulation studies involving hundreds of thousands of atoms, such as the F_1-ATPase on time scales of several seconds remains far out of reach.[64] For this reason, methods have

been developed where time-dependent external forces are applied to a system in order to sample large conformational changes that would normally be inaccessible on the time scale of typical MD simulations.[65] These types of methods are known as steered molecular dynamics (SMD) simulation methods.

1.4.1 Enforced Rotation

One specific example of a SMD method is that of enforced rotation.[66] This method can apply a variety of rotation potentials, either with a flexible or rigid local rotation axis, to a group of atoms. A flexible axis rotation was developed in efforts to describe a more realistic rotation of biomolecules such as F_1-ATPase.[66] This technique applies a torque to a flexible axis that fits an arbitrary shaped cavity such as the apical bearing of F_1-ATPase (Figure 1.6) and allows adaptation of the curved flexible axis. Flexible axis rotation is achieved by dividing the rotation group into equal sections or slabs that are perpendicular to the rotation vector. A separate rotation potential is applied to each slab to achieve adaptation to its rotation environment.

1.4.2 Center-of-Mass Pulling

Another, common method is the pulling method which is referred to as center-of-mass (COM) pulling in GROMACS.[40] This method applies a potential (represented as a spring) between the COM of one or more pairs of grouped atoms/molecules. This allows the user to "pull" a chosen group along a reaction coordinate. A reaction coordinate usually involves two pull groups where one is usually fixed, and the other is attached to a potential spring. To better understand this method, we will use the pulling of a peptide in an amyloid protofibril as an example (Figure 1.8).[67]

The Aβ_{42} protofibril (PDB code 2BEG) is made up of five peptides. As described by Lemkul and Bevan,[67] studying the interactions between these peptides is very important as it can reveal the features that contribute to their stability in the progression of Alzheimer's disease. To understand the stability of these peptides, one can look at free energies using COM pulling. By pulling on the fist peptide (blue in Figure 1.8) and keeping the second peptide (red in Figure 1.8) fixed, free energies can be calculated.

To do this, the pull groups need to be defined. The red peptide will serve as the first pull group (p_1) where it will be fixed using position restraining potentials. The blue peptide will be the second pull group (p_2) where a spring will be attached to its COM. The distance between p_1 and p_2 will determine the reaction coordinate (the direction p_2 will be pulled). A fixed directional velocity, $\mathbf{D}_{vel}$, is introduced to start the pulling simulation (Figure 1.8b). Once pulling starts, the spring will be stretched until protein-protein interactions between the two peptides can be overcome. The pulling of the spring attached to p_2 continues until the peptide is fully detached (Figure 1.8c). Through further analysis of forces associated with maximum spring stretching, the free energy of these two peptides can be calculated.[67]

The COM pulling serves useful not only for calculating free energies of molecules, but also exploring conformational states of proteins and other macromolecules. One can even use it to "pull" a group of atoms around an arbitrary rotation axis if the proper reaction coordinates are calculated. Overall, SMD methods help facilitate the simulations of conformational and dynamical movements of proteins while minimizing computational cost. These methods will prove vital for deciphering the mechanical properties of ATP synthase.

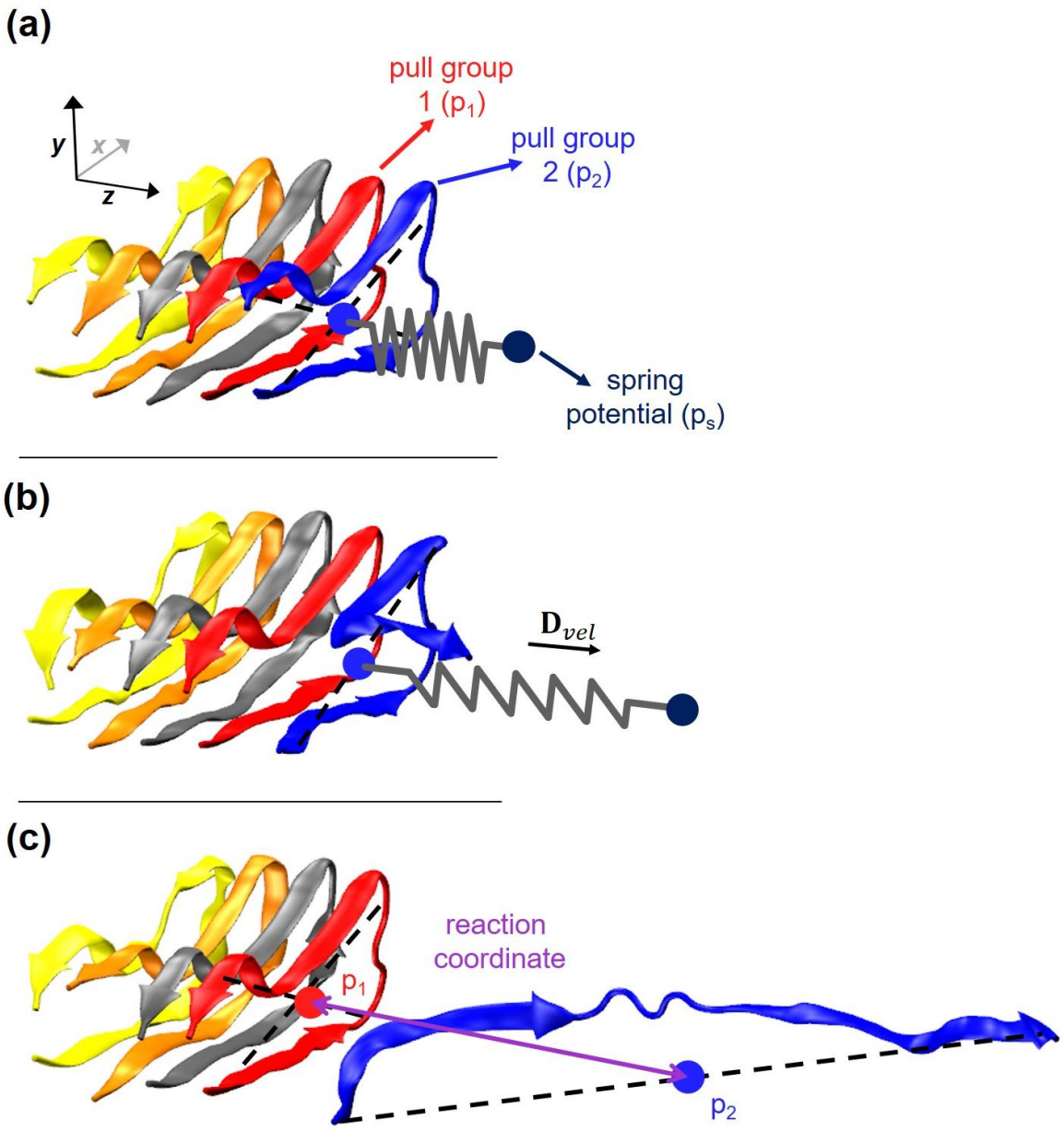

Figure 1.8 pulling of a peptide in Aβ_{42} protofibril.
(a) Initial state of the protofibril before pulling of peptide A (pull group 2: p_2 in blue). Peptide B is shown in red (pull group 1: p_1) and is position restrained during simulations. A potential spring (p_s) is attached to p_2. (b) Midpoint frame of pulling simulation showing stretched potential spring. $\mathbf{D}_{vel}$ is the velocity vector at which p_2 is being pulled away from p_1. (c) Final frame of pulling simulation, showing a better representation of the reaction coordinate made up of the distance between p_1 and p_2.

1.5 Scope of the Thesis

ATP synthase is a complex molecular machine that consists of more than 20 subunits. Some of these subunits are yet to be structurally resolved and therefore their functions are still unknown. Numerous experiments have been conducted to characterize the functionally relevant motions of catalytically active ATPase, but many atomistic details remain poorly understood. By pairing MD simulations with the existing experimental data outlined in section 1.2.2, we hope to obtain some of this missing information. We focus on modeling the F_1-ATPase of both bovine heart mitochondria and *E. coli* using MD simulations. We test and compare two SMD methods: (1) enforced bulk rotation and (2) the off-axis force rotation method developed here, which takes advantage of the COM pulling SMD in GROMACS package.

In the past, the rotation of the γ rotor has been dealt with by applying a torque to all of the γ subunit through the use of traditional enforced rotation MD methods. Our new method is designed to mimic the off-axis forces acting on γ during rotation. The trajectories of the production runs will be compared to HDX work from our laboratory on the dynamical stability of the γ subunit under physiological conditions.[6,7] The idea is to determine the reasons for the destabilization seen in the γ C-terminal helix during rotational motion, which is hypothesized to be caused by resistive forces ("friction") in the apical bearing region.[7] This will be done by examining the structural integrity of γ during rotation, as well as the properties of hydrogen bonds in the protein backbone. Experimentally, a destabilization of hydrogen bonds gives rise to enhanced HDX rates. For this reason, we hope that it will become possible to directly correlate our simulation results with the experimental HDX data obtained.[6,7] The current work marks the first time

that a combined MD/HDX approach has been applied to a motor protein. The findings obtained here have general implications for the behavior of rotor/bearing systems in molecular machines.

References

1. Walker, J. E. *Biochem. Soc. Trans.* **2013**, *41*, 1-16.
2. Gibbons, C.; Montgomery, M. G.; Leslie, A. G. W.; Walker, J. E. *Nat. Struct. Biol.* **2000**, *7*, 1055-1061.
3. Abrahams, J. P.; Leslie, A. G. W.; Lutter, R.; Walker, J. E. *Nature* **1994**, *370*, 621-628.
4. Bowler, M. W.; Montgomery, M. G.; Leslie, A. G. W.; Walker, J. E. *J. Biol. Chem.* **2007**, *282*, 14238-14242.
5. Cingolani, G.; Duncan, T. M. *Nat. Struct. Mol. Biol.* **2011**, *18*, 701-708.
6. Murcia Rios, A.; Vahidi, S.; Dunn, S. D.; Konermann, L. *J. Am. Chem. Soc.* **2018**, *140*, 14860-14869.
7. Vahidi, S.; Bi, Y. M.; Dunn, S. D.; Konermann, L. *Proc. Natl. Acad. Sci. U.S.A.* **2016**, *113*, 2412-2417.
8. Lu, P.; Lill, H.; Bald, D. *Biochim. Biophys. Acta* **2014**, *1837*, 1208-1218.
9. Zhang, A. T.; Montgomery, M. G.; Leslie, A. G. W.; Cook, G. M.; Walker, J. E. *Proc Natl Acad Sci U S A* **2019**, *116*, 4206-4211.
10. Zhou, A. N.; Rohou, A.; Schep, D. G.; Bason, J. V.; Montgomery, M. G.; Walker, J. E.; Grigorieff, N.; Rubinstein, J. L. *Elife* **2015**, *4*.
11. Sobti, M.; Smits, C.; Wong, A. S. W.; Ishmukhametov, R.; Stock, D.; Sandin, S.; Stewart, A. G. *Elife* **2016**, *5*.
12. Junge, W.; Lill, H.; Engelbrecht, S. *Trends Biochem.Sci.* **1997**, *22*, 420-423.
13. Junge, W.; Nelson, N. *Annu. Rev. Biochem.* **2015**, *84*, 631-657.
14. Bulygin, V. V.; Duncan, T. M.; Cross, R. L. *J. Biol. Chem.* **1998**, *273*, 31765-31769.
15. Kato-Yamada, Y.; Noji, H.; Yasuda, R.; Kinosita, K.; Yoshida, M. *J. Biol. Chem.* **1998**, *273*, 19375-19377.
16. Yasuda, R.; Noji, H.; Yoshida, M.; Kinosita, K., Jr.; Itoh, H. *Nature* **2001**, *410*, 898-904.
17. Masaike, T.; Koyama-Horibe, F.; Oiwa, K.; Yoshida, M.; Nishizaka, T. *Nature structural & molecular biology* **2008**, *15*, 1326-1333.
18. Nam, K.; Pu, J. Z.; Karplus, M. *Proc. Natl. Acad. Sci. U.S.A.* **2014**, *111*, 17851-17856.
19. Konermann, L.; Pan, J.; Liu, Y. *Chem. Soc. Rev.* **2011**, *40*, 1224-1234.
20. Okazaki, K.; Hummer, G. *Proc. Natl. Acad. Sci. U.S.A.* **2015**, *112*, 10720-10725.
21. Martin, J. L.; Ishmukhametov, R.; Hornung, T.; Ahmad, Z.; Frasch, W. D. *Proc. Natl. Acad. Sci. U.S.A.* **2014**, *111*, 3715-3720.

22. Noji, H.; Yasuda, R.; Yoshida, M.; Kinosita, K. *Nature* **1997**, *386*, 299-302.

23. Yasuda, R.; Noji, H.; Kinosita, K.; Yoshida, M. *Cell* **1998**, *93*, 1117-1124.

24. Hirono-Hara, Y.; Noji, H.; Nishiura, M.; Muneyuki, E.; Hara, K. Y.; Yasuda, R.; Kinosita, K.; Yoshida, M. *Proc. Natl. Acad. Sci. U.S.A.* **2001**, *98*, 13649-13654.

25. Adachi, K.; Oiwa, K.; Nishizaka, T.; Furuike, S.; Noji, H.; Itoh, H.; Yoshida, M.; Kinosita, K. *Cell* **2007**, *130*, 309-321.

26. Adachi, K.; Yasuda, R.; Noji, H.; Itoh, H.; Harada, Y.; Yoshida, M.; Kinosita, K. *Proc. Natl. Acad. Sci. U. S. A.* **2000**, *97*, 7243-7247.

27. Hilbers, F.; Junge, W.; Sielaff, H. *Plos One* **2013**, *8*.

28. Bowler, M. W.; Montgomery, M. G.; Leslie, A. G. W.; Walker, J. E. *Proc. Natl. Acad. Sci. U.S.A.* **2006**, *103*, 8646-8649.

29. Weber, J.; Wilkemounts, S.; Senior, A. E. *J. Biol. Chem.* **1994**, *269*, 20462-20467.

30. Karplus, M.; McCammon, J. A. *Nat. Struct. Biol.* **2002**, *9*, 646-652.

31. Pu, J.; Karplus, M. *Proc Natl Acad Sci U S A* **2008**, *105*, 1192-1197.

32. Mukherjee, S.; Warshel, A. *Proc. Natl. Acad. Sci. U.S.A.* **2011**, *108*, 20550-20555.

33. Okazaki, K.; Hummer, G. *Proc. Natl. Acad. Sci. U.S.A.* **2013**, *110*, 16468-16473.

34. Czub, J.; Grubmuller, H. *J. Am. Chem. Soc.* **2014**, *136*, 6960-6968.

35. Czub, J.; Wieczor, M.; Prokopowicz, B.; Grubmuller, H. *J. Am. Chem. Soc.* **2017**, *139*, 4025-4034.

36. Beck, D. A. C.; Daggett, V. *Methods* **2004**, *34*, 112--120.

37. Birdsall, C. K.; Langdon, A. B. *Plasma Physics via Computer Simulation*; CRC Press, 2004.

38. Verlet, L. *Phys. Rev.* **1967**, *159*, 98-103.

39. Martys, N. S.; Mountain, R. D. *Phys Rev E* **1999**, *59*, 3733-3736.

40. Abraham, M. J.; Murtola, T.; Schulz, R.; Páll, S.; Smith, J. C.; Hess, B.; Lindahl, E. *SoftwareX* **2015**, *1–2*, 19-25.

41. Kukol, A. *Molecular Modeling of Proteins*; Humana Press, 2015.

42. Cisneros, G. A.; Karttunen, M.; Ren, P. Y.; Sagui, C. *Chem. Rev.* **2014**, *114*, 779-814.

43. Jorgensen, W. L.; Chandrasekhar, J.; Madura, J. D.; Impey, R. W.; Klein, M. L. *J. Chem. Phys.* **1983**, *79*, 926-935.

44. Berendsen, H. J. C.; Grigera, J. R.; Straatsma, T. P. *J. Phys. Chem.* **1987**, *91*, 6269-6271.

45. Vega, C.; de Miguel, E. *J. Chem. Phys.* **2007**, *126*, 154707.

46. Jorgensen, W. L.; Madura, J. D. *Mol. Phys.* **1985**, *56*, 1381-1392.

47. Abascal, J. L. F.; Vega, C. *J. Chem. Phys.* **2005**, *123*, 234505.

48. Mahoney, M. W.; Jorgensen, W. L. *J. Chem. Phys.* **2000**, *112*, 8910-8922.

49. Jorgensen, W. L.; Tiradorives, J. *J. Am. Chem. Soc.* **1988**, *110*, 1657-1666.

50. MacKerell, A. D.; Bashford, D.; Bellott, M. L. D. R.; Dunbrack, R. L.; Evanseck, J. D.; Field, M. J.; Fischer, S.; Gao, J.; Guo, H.; Ha, S. A. *J. Phys. Chem. B* **1998**, *102*, 3586-3616.

51. Cornell, W. D.; Cieplak, P.; Bayly, C. I.; Gould, I. R.; Merz, K. M.; Ferguson, D. M.; Spellmeyer, D. C.; Fox, T.; Caldwell, J. W.; Kollman, P. A. *J. Am. Chem. Soc.* **1995**, *117*, 5179-5197.

52. Ewald, P. P. *Annalen der Physik* **1921**, *369*, 253-287.

53. Essmann, U.; Perera, L.; Berkowitz, M. L.; Darden, T.; Lee, H.; Pedersen, L. G. *J. Chem. Phys.* **1995**, *103*, 8577-8593.

54. Darden, T.; York, D.; Pedersen, L. *J. Chem. Phys.* **1993**, *98*, 10089-10092.

55. Berendsen, H. J. C.; Postma, J. P. M.; Vangunsteren, W. F.; Dinola, A.; Haak, J. R. *J. Chem. Phys.* **1984**, *81*, 3684-3690.

56. Andersen, H. C. *J. Chem. Phys.* **1980**, *72*, 2384-2393.

57. Nose, S. *Mol. Phys.* **1984**, *52*, 255-268.

58. Hoover, W. G. *Phys. Rev. A* **1985**, *31*, 1695-1697.

59. Bussi, G.; Donadio, D.; Parrinello, M. *J. Chem. Phys.* **2007**, *126*, 0141011-0141017.

60. Parrinello, M.; Rahman, A. *J. Appl. Phys.* **1981**, *52*, 7182-7190.

61. Ryckaert, J.-P.; Ciccotti, G.; Berendsen, H. J. C. *J. Comput. Phys.* **1977**, *23*, 327-341.

62. Miyamoto, S.; Kollman, P. A. *J. Comput. Chem.* **1992**, *13*, 952-962.

63. Hess, B.; Henk, B.; Berendsen, H. J. C.; Fraaije, J. G. E. M. *J. Comput. Chem.* **1997**, *18*, 1463-1472.

64. Piana, S.; Lindorff-Larsen, K.; Shaw, D. E. *Proc. Natl. Acad. Sci. U.S.A.* **2013**, *110*, 5915-5920.

65. Izrailev, S.; Stepaniants, S.; Isralewitz, B.; Kosztin, D.; Lu, H.; Molnar, F.; Wriggers, W.; Schulten, K.; Springer Berlin Heidelberg: Berlin, Heidelberg, 1999, pp 39-65.

66. Kutzner, C.; Czub, J.; Grubmuller, H. *J. Chem. Theory Comput.* **2011**, *7*, 1381-1393.

67. Lemkul, J. A.; Bevan, D. R. *J. Phys. Chem. B* **2010**, *114*, 1652-1660.

2 Evidence for a Partially Stalled γ Rotor in F1-ATPase from H/D Exchange Experiments and Molecular Dynamics Simulations[1]

2.1 Introduction

F_OF_1 is a membrane-bound molecular motor that is capable of using proton-motive force (PMF) to synthesize adenosine triphosphate (ATP) from adenosine diphosphate (ADP) and inorganic phosphate.[1-4] The *E. coli* system has the subunit composition $\alpha_3\beta_3\gamma\delta\varepsilon ab_2c_{10}$, where $\gamma\varepsilon c_{10}$ represents the central rotor. The membrane-embedded c_{10} ring forms the basal rotor end. At the opposite (apical) end of the rotor, the γ C-terminal helix reaches into the catalytic head where $\alpha_3\beta_3$ forms an apical bearing (Figure 2.1a).[1,2,5-12] Under ATP hydrolysis conditions the rotation of $\gamma\varepsilon c_{10}$ is driven by movements of the β-levers that apply off-axis forces to γ.[12,13] Each β catalytic site successively switches through three states ($\beta_{ATP} \rightarrow \beta_{ADP} \rightarrow \beta_{empty} \rightarrow ...$),[14] and each of these transitions advances $\gamma\varepsilon c_{10}$ by 120°.[2,15-17] Rotation of c_{10} causes vectorial proton transport.[9,12,18,19]

Experiments and molecular dynamics (MD) simulations have uncovered many of the principles underlying F_OF_1 operation.[1,2,5-13,16,20,21] Nonetheless, the exact conformational transitions of individual subunits during rotational catalysis remain incompletely understood. These knowledge gaps arise from the fact that static crystallographic and

---

[1] Reproduced in part from **Murcia Rios, A.**, Vahidi, S., Dunn S. D. & Konermann, K. (2018) Evidence for a Partially Stalled γ Rotor in F_1-ATPase from Hydrogen-Deuterium Exchange Experiments and Molecular Dynamics Simulations. *J. Am. Chem. Soc.* 140:14860.

cryo-EM data do not reveal all of the mechanistically important movements. Spectroscopic tools can provide insights into such dynamic features, but the structural resolution of those experiments tends to be limited.[5,6,16,22-27]

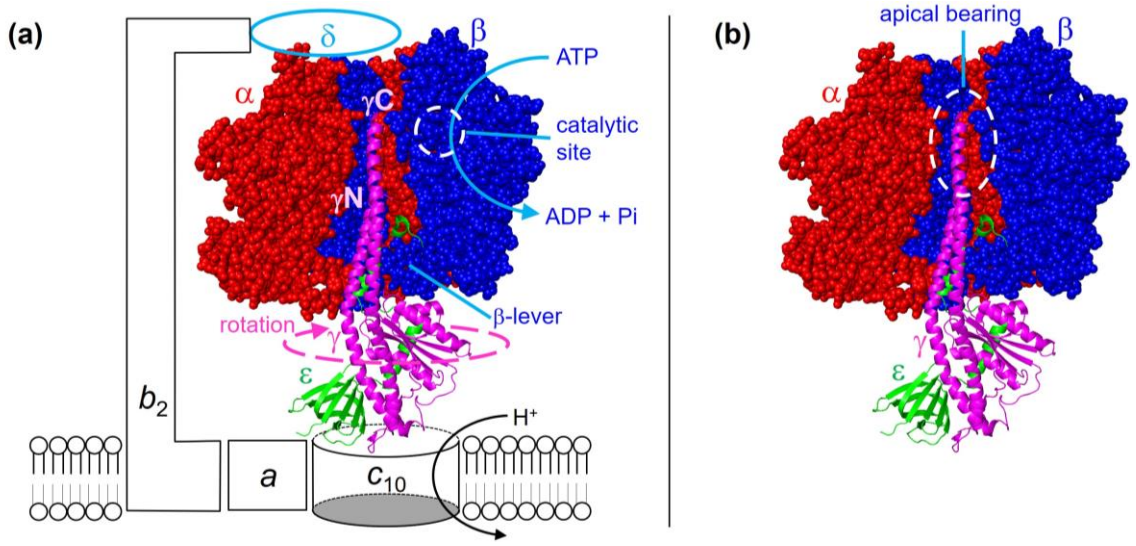

Figure 2.1 F_OF_1 ATP synthase structure representation.
(a) *E. coli* F_OF_1 architecture based on PDB file 3OAA.[12,13] One αβ pair facing the observer has been omitted to expose the γ rotor (termini of the γ are denoted as γN and γC). Catalytic site and β-lever are highlighted for one of the three β subunits. (b) F_1-ATPase. The figure highlights the apical bearing, where the γ C-terminal helix is seated within the $\alpha_3\beta_3$ head. Reproduced with permission. Copyright © 2018, American Chemical Society.

Hydrogen deuterium exchange (HDX) mass spectrometry (MS) can probe dynamic motions of proteins.[28-36] Backbone amide deuteration in folded regions is mediated by H-bond opening/closing fluctuations.[37,38] At pH 8 (which is commonly used for F_OF_1 studies[39,40]) the intrinsic exchange of unprotected amides occurs with $k_{int} \approx 10\ s^{-1}$ at room temperature.[41] Protein dynamics associated with closing events much faster than k_{int} give rise to EX2 conditions, where isotope envelopes gradually shift to higher mass. Conversely, the EX1 regime is characterized by closing rates much slower than k_{int}. Such EX1 dynamics usually take place in the form of cooperative (collective) fluctuations that give rise to bimodal isotope envelopes.[32,42-44]

We recently applied HDX-MS to F_OF_1.[40] The γ C-terminal helix exhibited elevated deuteration during ATP hydrolysis-driven rotation. We attributed this effect to torsional stress arising from rotor over-twisting, mediated by the interplay of β-lever action and friction-like $\gamma\cdots\alpha_3\beta_3$ contacts in the apical bearing. This destabilization of γ was observed only during operation against a PMF-induced torque; the effect disappeared when PMF was eliminated by an uncoupler. We noted[40] that this behavior is analogous to that of macroscopic powertrains, where bearings inflict greater forces on the drive shaft when a motor is under load than during idling.[45] However, the role of friction-related phenomena in molecular motors remains controversial,[20,24,46] and the understanding of such effects in F_OF_1 is rudimentary.[40]

Unravelling the inner workings of F_OF_1 is complicated by its many interacting subunits and PMF-energized membrane. F_1-ATPase is a water soluble F_OF_1 subcomplex. It represents a more tractable system that retains the ability to drive γ rotation via ATP hydrolysis.[16,23-27,47] F_1-ATPase from *E. coli* has the composition $\alpha_3\beta_3\gamma\delta\varepsilon$[14,17,48-51] (MW 382 kDa, Figure 2.1b).[5,27] Due to the lack of a c_{10} ring, the "foot" of γ protrudes into the solvent. Because of its reduced size F_1-ATPase is well suited for exploring the conformational dynamics of the γ rotor, and the role of $\gamma\cdots\alpha_3\beta_3$ contacts in the apical bearing. It has traditionally been envisioned that hydrophobic residues lining the inside of the apical bearing allow smooth rotation of the γ C-terminal helix (together with the rest of γ).[14] Interestingly, Hilbers *et al.*[52] recently demonstrated that γ rotation in F_1-ATPase still takes place after disulfide linking the γ C-terminal helix with $\alpha_3\beta_3$. Thus, F_1-ATPase can function with a stalled ("stuck") apical rotor tip, via local unfolding of the γ C-terminal helix with swivel rotation around ϕ/ψ angles.[52] The implications of those

findings[52] for unmodified F_1-ATPase are unclear. It remains to be established if all parts of γ participate in rotation under normal operating conditions.

In the present study we conducted the first HDX-MS investigation of F_1-ATPase. Our work employed working/inhibited state comparisons. To distinguish trivial substrate binding effects from features that are uniquely linked to rotation we examined three non-rotating states. (i) The ADP-inhibited state I_{ADP} has Mg·ADP and azide permanently bound in at least one catalytic site.[25,53] (ii) $I_{AMP\text{-}PNP}$ represents a state where the enzyme binds azide and the non-hydrolyzable substrate analog AMP-PNP.[53] (iii) The Mg^{2+}-depleted state $I_{Mg\text{-}dep}$ represents F_1-ATPase that is essentially nucleotide-free because its nucleotide binding affinity is reduced by orders of magnitude.[54] (iv) In addition to these three inactive states we characterized the working state *W* where F_1-ATPase underwent ATP hydrolysis-driven γ rotation.

The HDX-MS experiments of this work were complemented by all-atom steered MD simulations[55-57] designed to mimic the off-axis forces acting on γ during rotation. HDX-MS revealed significant destabilization of H-bonds in the γ C-terminal helix during rotational catalysis. MD simulations uncovered that this effect arises from occasional stalling of the over-twisted helix in the apical bearing. Our data imply that movement of γ within the apical bearing is associated with significant rotational resistance, very different from the previously envisioned "hydrophobically greased"[14,58] rotation. The current work marks the first time that a combined MD/HDX approach was applied to a motor protein. The findings obtained have general implications for the behavior of rotor/bearing systems in molecular machines.

2.2 Methods

All-atom MD runs were conducted using Gromacs 2016.4 with GPU acceleration,[59] the CHARMM36 force field, [60] and TIP3P water.[61] Most simulations were conducted on the *E. coli* $\alpha_3\beta_3\gamma$ complex (3OAA, structure #1).[13] Mg·AMP-PNP in the three noncatalytic α-sites was modified to Mg·ATP.[13] In 3OAA the β_{TP} and β_E sites are empty, while the β_{DP} site is occupied by Mg·ADP. Unless noted otherwise, simulations were conducted with nucleotides bound only to the noncatalytic sites. Additional runs were conducted with one or two nucleotides bound to the catalytic sites. Missing residues and side chains were inserted using PyMOL. The extended N-terminal tails of α (α1-26) were truncated to reduce the size of the simulation box. To avoid rotation of the entire complex and to mimic the immobilization technique used in some experiments[16,23-27,47] the N-terminal crown of the three β subunits (β9-80) was restrained[17,57] using a force constant of 1000 kJ mol^{-1} nm^{-2}.

All run conditions were initially tested and validated using bovine $\alpha_3\beta_3\gamma$ F_1-ATPase (1E79)[62] which had been used for previous simulations.[17,48,63] For implementing periodic boundary conditions F_1-ATPase was centered in a box with a minimum distance of 1 nm from the edges. Titratable sites were set to their canonical charge states. The Verlet cut-off scheme was used for neighbor search with 1 nm electrostatic and van der Waals cut-offs, and with particle mesh Ewald summation for long-range electrostatics.[64] 150 mM NaCl was added and additional ions were included to make the system neutral. After steepest descent energy minimizations the system was NVT and NPT equilibrated (1 bar, 310 K, 100 ps each) using a velocity-rescaling thermostat[65] and Parrinello-Rahman barostat.[66] Initial velocities were sampled from a Maxwell-Boltzmann distribution. NPT

production runs were performed starting from the equilibrated system with the Nosé-Hoover[67] thermostat at 310 K and 1 bar with a 2 fs time step. Bonds were constrained using the linear constraint solver algorithm.[68]

Steered MD was applied to drive rotation of γ by 120°. Two different protocols were applied: (1) *Enforced bulk rotation* was conducted in a rhombic dodecahedral box (~313,000 atoms) using the flex2-t flexible axis method of Grubmüller (Figure 2.2a).[69,70] Within this approach γ was divided into 1.5 nm thick slabs that were perpendicular to the rotation vector defined by the longest principal axis of the $\alpha_3\beta_3$ stator. A rotation potential with a force constant of 400 kJ mol^{-1} nm^{-2} and a rotation rate of 21° ns^{-1} was applied to all atoms in each slab. Hence, all of γ served as rotation group,[69,70] and each γ residue was forced to move on a circular trajectory.

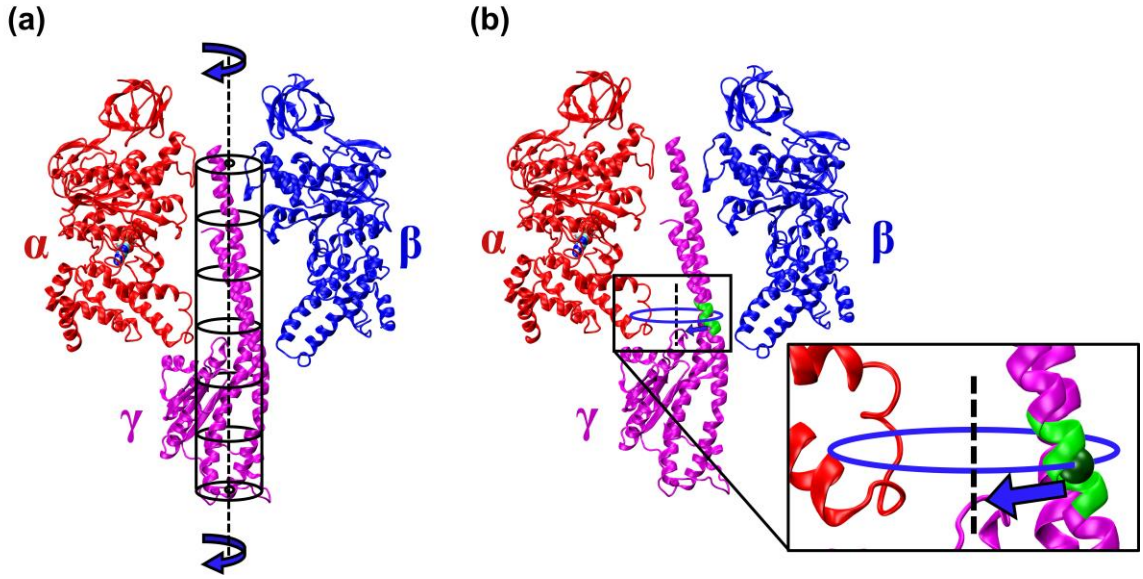

Figure 2.2 Schematic depiction of two different steered MD strategies used to drive a 120° rotation of γ in F_1-ATPase.
(a) Enforced bulk rotation, where forces are applied to all residues of γ. (b) Off-axis force rotation, where forces are applied only to γ20-26 (green), mimicking the action of β-lever power strokes. The blue circle in (b) indicates the γ20-26 trajectory. All simulations were performed on the $\alpha_3\beta_3\gamma$ complex; two α and two β chains are not shown to reduce clutter. The β subunit depicted here is β_{empty}, which is poised to bind ATP and initiate the power stroke. Reproduced with permission. Copyright © 2018, American Chemical Society.

(2) For this work we also developed an *off-axis force* algorithm that employed center-of-mass (COM) pulling[56] in a cubic box (~787,000 atoms). To mimic a β-lever-mediated power stroke, residues γ20-26[17,71] were subjected to a pulling force (Figure 2.2b).[17,57] This was achieved by applying a harmonic potential with a force constant of 1000 kJ mol^{-1} nm^{-2} to the γ20-26 COM. Pulling speeds along a directional vector **D** were between 2.2 nm ns^{-1} and 0.15 nm ns^{-1}. Proper movement of γ20-26 was achieved by updating **D** in 10 ps intervals. The three C_α atoms of residues β11 (β19 for bovine F_1) represented the reference group. The normal vector at the center of the plane defined by the reference group served as rotation axis. In this way, the COM of γ20-26 was forced to move around this axis on a circular trajectory along pre-defined points (see

Figure 2.3 for details). The trajectory radius was (1.4 ± 0.1) nm, where the ± variation reflects the slightly different locations of the γ20-26 COM after equilibration. For smooth trajectories the specified pulling speeds would provide rotation rates between 91˚ ns^{-1} and 5.6˚ ns^{-1}. However, directional fluctuations increased the time required to complete the runs. Actual rotation rates were between 29˚ ns^{-1} and 3.3˚ ns^{-1}. These conditions are well within the range of γ rotation rates used for previous simulations which include 120˚ ns^{-1},[57] 20˚ ns^{-1},[17,69] 1-10˚ ns^{-1},[20] 3˚ ns^{-1},[63] and 0.42˚ ns^{-1}.[70] No restraints were applied to γ during off-axis force simulations.

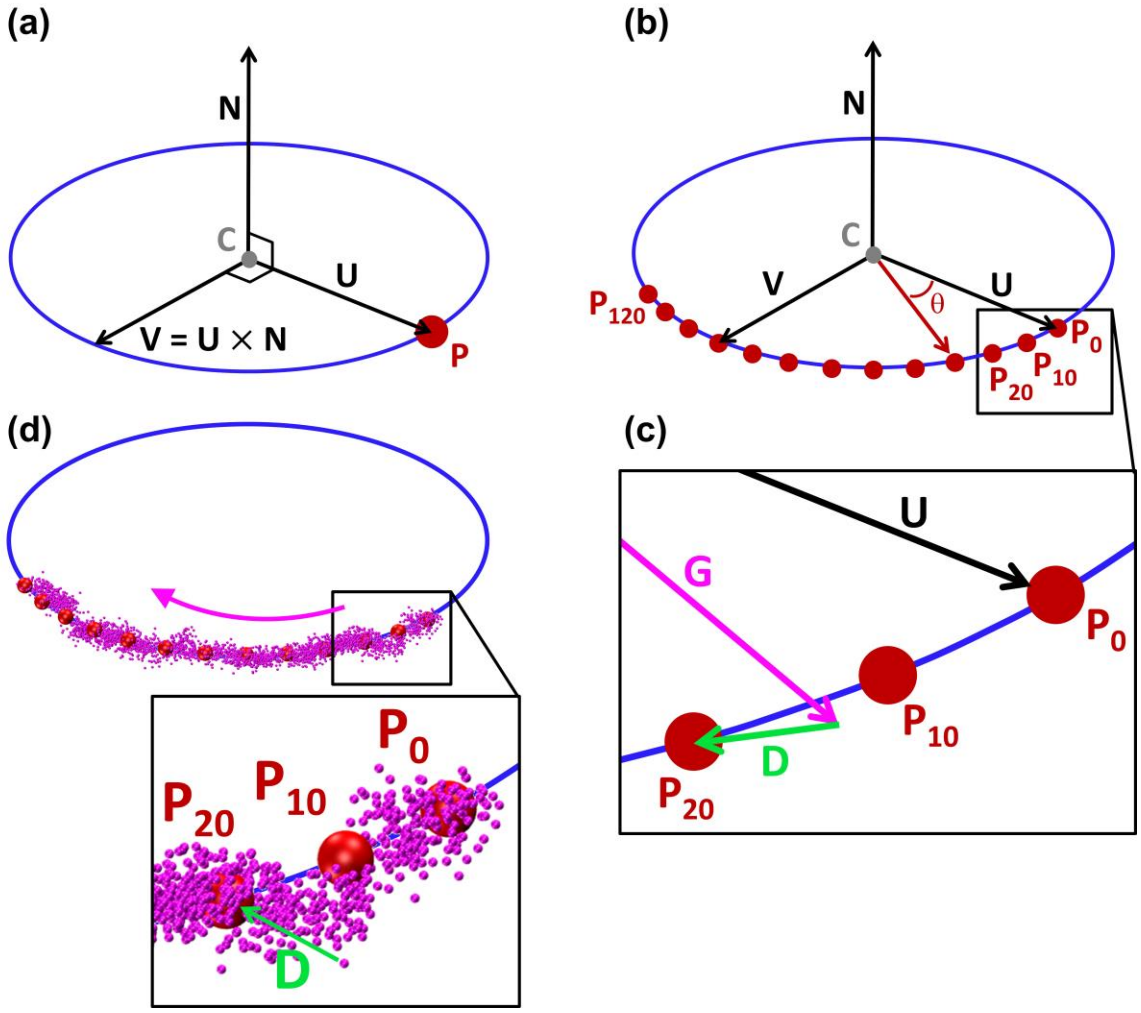

Figure 2.3 Details of the algorithm used for off-axis force rotation of γ by 120°.
(a) The general parametric equation of a circle is **P** = **C** + **U**cos(θ)R +**V**sin(θ)R, where **N** is the rotation axis and **C** defines the center of the circle. **U** is a unit vector that is orthogonal to **N**, and **V** = **U** × **N** is a unit vector that is orthogonal to both **U** and **N**. R is the radius, and θ describes the angle. (b) As θ increases, the point **P** moves along the circumference of the circle. For describing the rotation of γ20-26 within the $\alpha_3\beta_3\gamma$ complex, the three Cα atoms of residues β11 (β19 for bovine F_1) defined a plane, and **N** was the normal vector at the center of this plane. 12 target points $\mathbf{P_i}$ were calculated that were positioned on a 120° arc along the circumference. The starting point, $\mathbf{P_0}$, represented the initial position of γ20-26, as defined by the $\alpha_3\beta_3\gamma$ conformation after equilibration. Similarly, this equilibrated structure defined **N** and R. The subsequent target positions $\mathbf{P_{10}}$, $\mathbf{P_{20}}$, ... $\mathbf{P_{120}}$ were spaced in 10° intervals. (c) **G** represents the position of the γ20-26 COM at any point during the simulation. The pulling vector **D** defined the direction of the force that pulls **G** toward the next $\mathbf{P_i}$. Due to the interplay of pulling forces, reaction forces, and thermal motions, the movement of **G** during each $\mathbf{P_i} \rightarrow \mathbf{P_i}$+10 segment did not follow a straight line. Hence, the direction of **D** was updated in 10 ps intervals. (d) Actual trajectory of **G** during a 3.9° ns^{-1} off-axis force simulation. Reproduced with permission.

2.3 Results and Discussion

2.3.1 Enforced Bulk Rotation Simulations

For complementing our HDX-MS data we conducted steered MD simulations[55-57] on F_1-ATPase. As in previous work, 120° rotation segments of γ were modeled within the $\alpha_3\beta_3\gamma$ complex.[17,20,48,49,57,63,69-75] Subunits δ and ε (which do not participate in F_1 power transmission) were omitted.[2,16] While allowing for some torsional elasticity of γ,[2] previously used MD protocols forced γ to maintain conformations relatively close to the crystal structure. In addition, previous work used restraints to keep the rotation axis close to the $\alpha_3\beta_3$ centerline.[17,57,63,69] Such heuristic restraints promote stable simulation runs, but they likely paint an overly restrictive picture of the conformational freedom experienced by γ.

For illustrative purposes we initially simulated the behavior of γ using enforced bulk rotation, which represents a well-established restrained protocol.[69,70] Under this scheme, γ experienced a global torque resulting from forces that were applied simultaneously to all γ residues (Figure 2.2a). By design, this algorithm caused the entire γ subunit to perform a 120° turn without major deformation (Figure 2.4a-c). The γ C-terminal helix rotated with the rest of γ (Figure 2.4d) and without disruption of its H-bonding network (Figure 2.5a, b). The $\alpha_3\beta_3$ head smoothly accommodated rotation of γ by passively moving β-levers, apical bearing side chains, and other segments. We do not dispute the usefulness of such enforced bulk rotation simulations for exploring certain aspects of $\alpha_3\beta_3\gamma$ operation.[48,63,69,70,75] However, this approach did not reproduce the HDX-detected destabilization of the γ C-terminal helix (Figure 1.7).

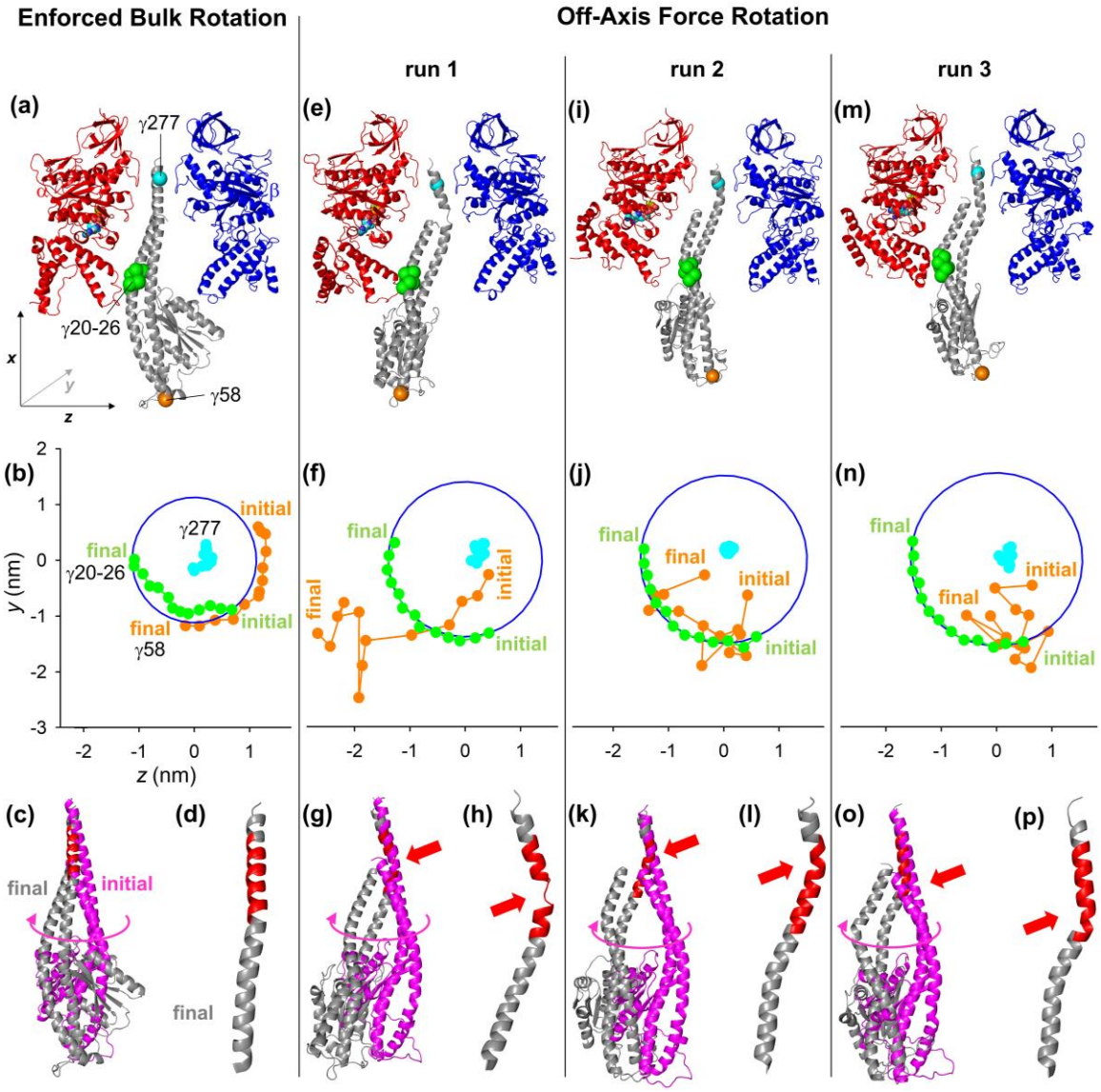

Figure 2.4 MD results for *E. coli* F_1-ATPase.
120° simulation were conducted on $\alpha_3\beta_3\gamma$. Not all subunits are shown to reduce clutter. (a-d) Enforced bulk rotation of γ. (e-p) γ Rotation by off-axis force simulations: run 1 at 3.9˚ ns^{-1}, run 2 at 3.3˚ ns^{-1}, run 3 at 4.8˚ ns^{-1}. Top row: final (120°) structures; Second row: y/z trajectories of γ segments: γ277 at the top of the γ C-terminal helix (cyan), γ58 at the base of γ (orange), and γ20-26 (green, pulling group for off-axis force rotation). Blue circles indicate expected γ20-26 trajectories. Third row: initial (magenta) and final (gray) γ conformations and orientations. Bottom row: C-terminal segment γ236-284 at the end of the MD runs. Arrows indicate MD-predicted H-bond opening during off-axis force rotation. The segments above these arrows were stalled ("stuck") and did not participate in γ rotation. Red color in the bottom row highlights regions that showed enhanced HDX during rotation (cf. Figure 1.7). Reproduced with permission. Copyright © 2018, American Chemical Society.

2.3.2 Off-Axis Force Simulations

The MD strategy used in the preceding paragraph does not reflect the actual forces experienced by γ in F_1-ATPase. Under *in vitro* conditions, γ rotation is driven by β-lever power strokes that apply *off-axis* forces to relatively few residues in the γ coiled coil.[16,17,57,76] Karplus[17] proposed an off-axis force method for modeling this type of torque generation. While Karplus' method[17] represented a major advance, it employed a stabilizing plastic network to minimize deformation of γ. Additional restraints were applied to eliminate tilting of the rotation axis.[17] As pointed out before, such restraints likely mask some of the conformational flexibility associated with rotational catalysis.

Here we devised an off-axis force method similar to that of Karplus,[17] except that deformation and tilting of γ were not suppressed by restraints. Rotation was driven by COM pulling[56] of γ20-26 which represents the key γ/β interaction region during power strokes.[57] Figure 2.4e-p displays data from three off-axis force runs. In each case, γ20-26 rotated along the expected 120° arc, together with parts of the γ coiled coil. The trajectories of other γ segments were less orderly and varied from run to run. The γ foot exhibited considerable lateral movement (exemplified by the orange trace of Figure 2.4f), implying that γ did not rotate on a stable axis. This behavior reflects the interplay of COM pulling forces and reaction forces exerted by $\alpha_3\beta_3$, keeping in mind that F_1-ATPase lacks a c_{10} bearing that would stabilize rotation of γ (Figure 2.1).

Importantly, the end of the γ C-terminal helix did not rotate in any of the off-axis force simulations, i.e., it remained stuck (stalled) in the apical bearing (Figure 2.4g, k, o). At the conclusion of the 120° runs, the (non-rotating) end of the γ C-terminal helix was

separated from the (rotating) lower part by a kink in the over-twisted helix (Figure 2.4h, l, p). These rotation-induced kinks caused H-bonds in the γ C-terminal helix to dissociate (Figure 2.5c-e).

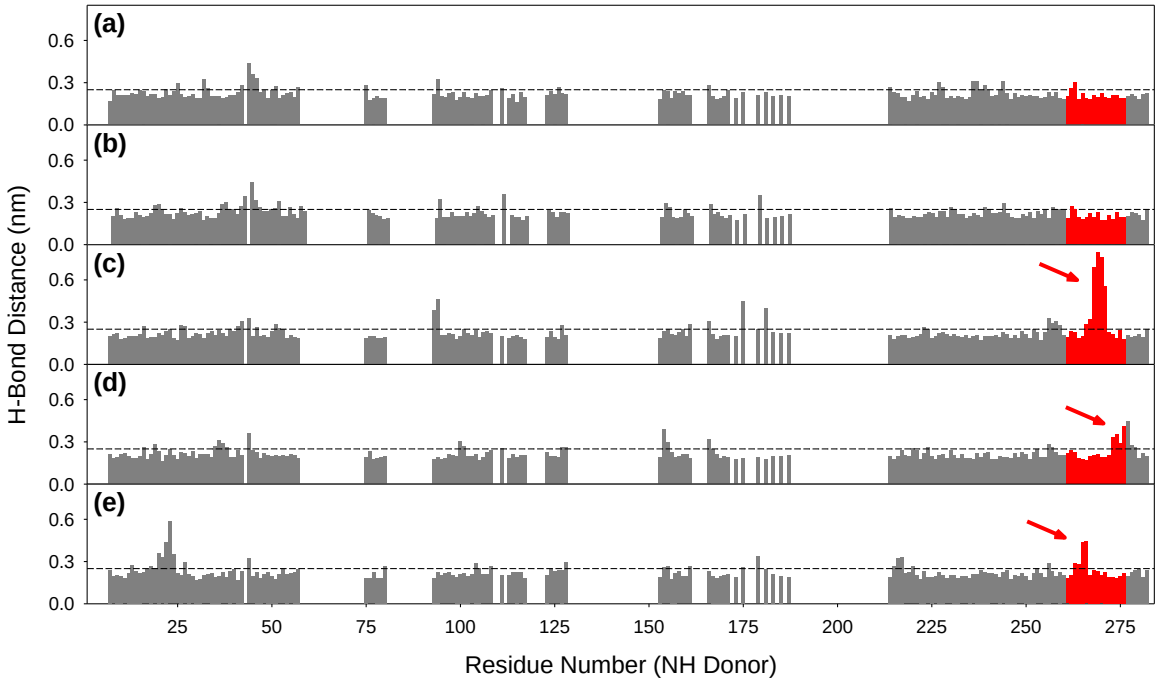

Figure 2.5 Backbone NH···OC distances in γ from MD simulations.
Values > 0.25 nm (dashed horizontal line)[77] represent disrupted H-bonds. Only NH sites that are H-bonded in the crystal structure are included. (a) Equilibrated structure prior to rotation. (b) After 120° enforced bulk rotation. (c) After 120° off-axis force rotation, run 1 at 3.9˚ ns^{-1}. (d) Ditto, run 2 at 3.3˚ ns^{-1}. (e) Ditto, run 3 at 4.8˚ ns^{-1}. Arrows highlight H-bond opening predicted in off-axis force simulations. Red indicates regions of enhanced deuteration in HDX experiments (cf. Figure 1.7d, f). Reproduced with permission.

Each of the three off-axis force runs triggered H-bond opening in slightly different positions close to the end of the γ C-terminal helix. Gratifyingly, all these opening events were located in the γ region that exhibited strongly enhanced HDX under *W* conditions (Figure 2.5c-e, Figure 1.7). Thus, HDX experiments and MD simulations independently identified the same segment of the γ C-terminal helix as being destabilized during rotation. The MD simulations did not predict any other major H-bond disruption,

consistent with the HDX data which did not indicate any other deuteration hot spots in γ (Figure 4d, f). Our MD data were further corroborated in simulations on *E. coli* and bovine F_1-ATPase using various nucleotide occupancies and rotation speeds, attesting to the robustness of our results (Figure 2.6, Figure 2.7).

2.3.3 Behavior of the Apical Bearing

When considered in isolation, the interpretation of HDX data (Figure 1.7) may be open to debate. In contrast, our MD trajectories provide unequivocal insights into the reasons underlying the opening of H-bonds in the γ C-terminal helix. These H-bonds rupture because the apical end of the rotor tends to stall in the apical bearing, while power strokes force the rest of γ to rotate. These conditions give rise to over-twisting of the γ C-terminal helix, resulting in transient unfolding of the rotor shaft. The unfolding events take place where the γ coiled coil transitions into a single helix, i.e., where the rotor is most fragile (Figure 2.4e, i, m). Taken together, our HDX experiments and MD simulations provide a consistent view of the destabilizing factors experienced by the γ C-terminal helix.

Previous work implied that the hydrophobic nature of the $\gamma\cdots\alpha_3\beta_3$ interface in the apical bearing would provide a low friction environment that facilitates rotation of the γ C-terminal helix.[14] The current results imply that this classical "greasy bearing" model[14,58] has to be revised. Our MD data demonstrate that hydrophobic contacts and steric clashes of nonpolar side chains interfere with smooth rotation of the γ C-terminal helix. Examples of such contacts include γ(I272/L276/V280) with β(M261/P262/V265), illustrated in Figure 2.7. Side chain H-bonds and salt bridges dissociate more readily and do not impede rotation to the same extent (Figure 2.7).

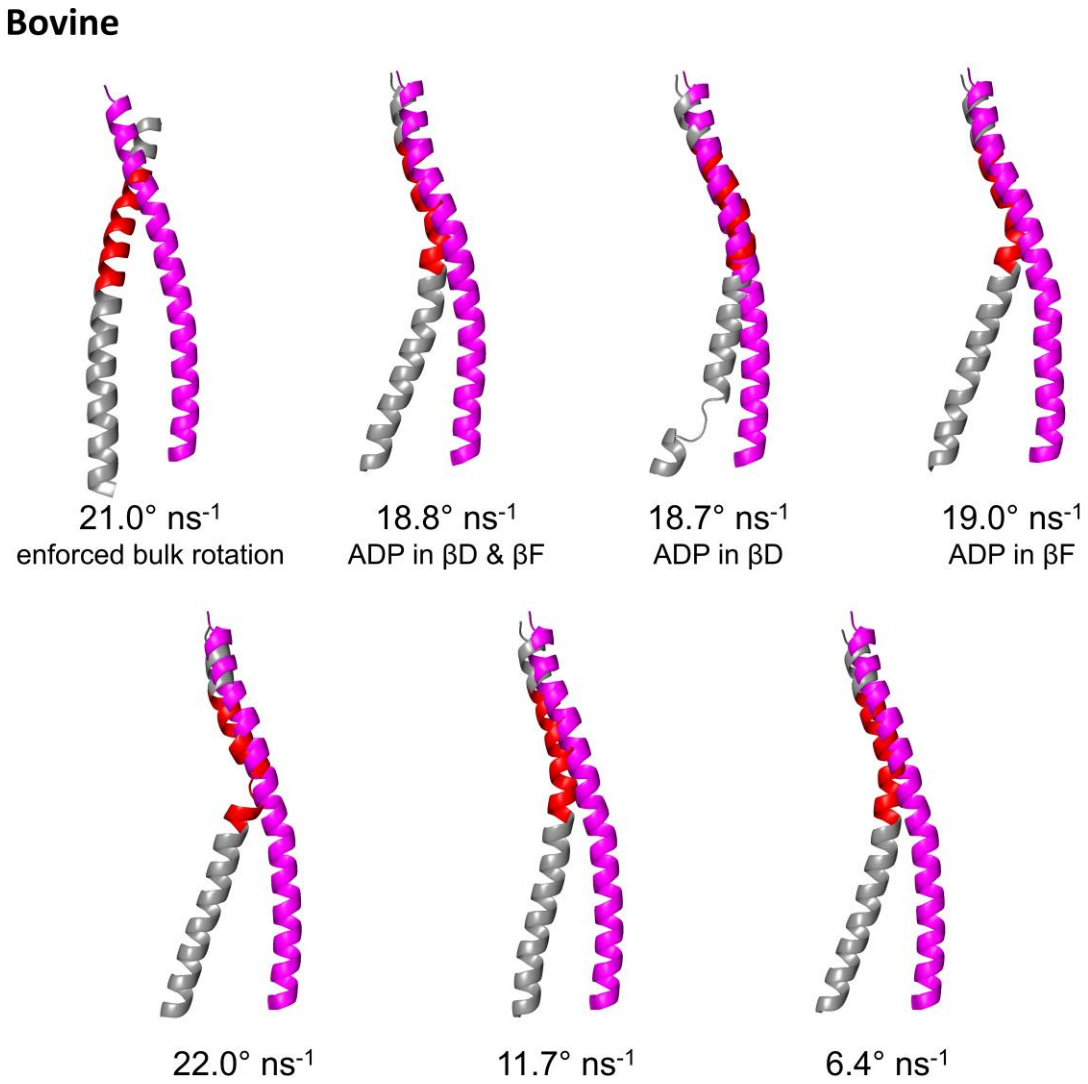

Figure 2.6 MD simulation results, highlighting the behavior of the γ C-terminal helix.

The data shown here are for bovine F_1-ATPase. Each panel shows the superposition of the equilibrated starting structure (magenta), and the final structure after the 120° run (gray). Rotation speeds are indicated. The three ATP molecules in the α noncatalytic sites were included for all runs. The presence of additional nucleotides is as indicated. Top left panel: Enforced bulk rotation, where the γ C-terminal helix rotated along with the remainder of γ. All other panels: Off-axis force rotation, where the upper tip of the γ C-terminal helix got "stuck" in the stalled apical bearing. Conspicuous kinks in the gray helices separate the non-rotating (upper) part from the over-twisted rotating (lower) part. Red indicates regions of enhanced deuteration, as seen in HDX experiments. Reproduced with permission.

What are the implications of our combined HDX/MD data for the mechanism of γ rotation in F_1-ATPase? At short HDX times the γ C-terminal helix under *W* conditions only shows a minor (< 1%) high mass EX1 component. This finding demonstrates that the steady-state population of F_1-ATPase molecules with an intact γ C-terminal helix is on the order of 99%. In other words, at any instant only a fraction of the catalytically active (*W*) F_1-ATPase complexes possess a disrupted γ rotor. The EX1 nature of the γ HDX kinetics implies that the catalytically active complexes only occasionally transition into the unfolded γ conformation (with $k_{op} \approx 0.01$ min^{-1}). They remain in this state for time periods longer than k_{int}^{-1} (≈ 0.1 s), and then switch back to the intact rotor structure.[32,42-44] It is possible that these refolding events take place after γ has completed a 360° rotation, such that the residues of the disrupted rotor tip are once again pre-aligned to assemble into an intact γ C-terminal helix.

Critics might argue that the HDX-detected *occasional* unfolding of γ differs from the MD simulations where *each* power stroke resulted in opening of the γ C-terminal helix. We attribute this discrepancy to the different rotation rates, *i.e.*, ~3° ns^{-1} in the MD runs vs. ~3×10^{-4} ° ns^{-1} under experimental conditions.[16] The slower rotation in the experiments provides more time for clashing side chains in the apical bearing to sample conformations that facilitate rotational gliding of the torsionally strained helix during power strokes.[20] Phenomenologically, this gliding will resemble the behavior seen in enforced rotation runs (Figure 2.5a-d / Figure 2.7a). It would be desirable to confirm this time dependence by conducting off-axis force MD runs at much lower rotation rates, but unfortunately such endeavors are not feasible due to their enormous computational cost. As noted, the rotation rates employed here are within the range used for previous

investigations.[17,20,57,63,69,70] Despite the difference in time scale, it is remarkable how well the MD-predicted H-bond opening events agree with the experimentally detected HDX hot spot in the γ C-terminal helix (Figure 2.5c-e).

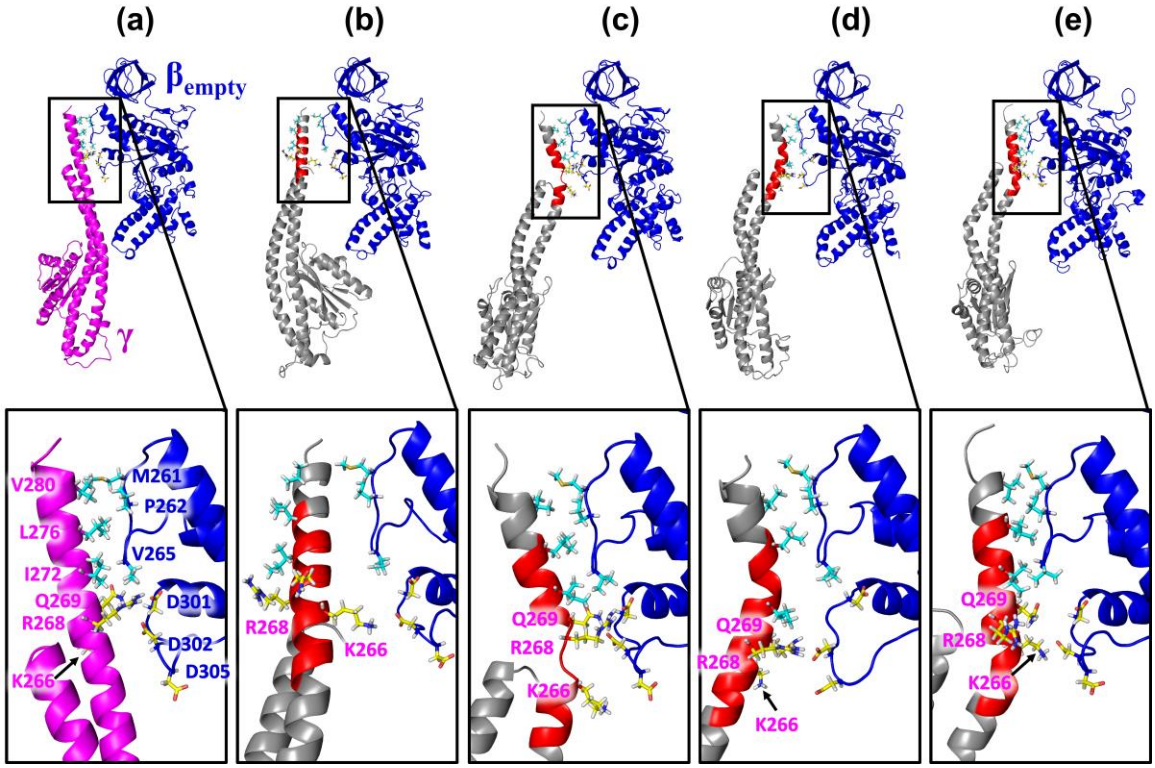

Figure 2.7 MD data for *E. coli* F_1-ATPase, highlighting interactions of the γ C-terminal helix with one of the β subunits in the apical bearing under various simulation conditions.

(a) Equilibrated starting structure. (b) After 120° enforced bulk rotation. (c) After 120° off-axis force rotation, run 1 at 3.9˚ ns^{-1}. (d) Ditto, run 2 at 3.3˚ ns^{-1}. (e) Ditto, run 3 at 4.8˚ ns^{-1}. Rotation of the γ C-terminal helix tip only takes place under the simulation conditions of (b), which do not properly reflect the forces acting on γ as explained in the main text. Rotation of the helix tip does not take place in under the conditions of (c), (d), (e), which provide a more realistic view of the forces acting during a power stroke. Note that the orientation of γ hydrophobic residues in (c), (d), (e) remains similar to that of the starting structure (a). Red coloring of the γ C-terminal helix in (c), (d), (e) represents the region that undergoes enhanced deuteration in HDX experiments during rotational catalysis. Reproduced with permission. Copyright © 2018, American Chemical Society.

2.4 Conclusion

Steered MD protocols and related modeling approaches have previously been applied to ATPases,[17,20,48,49,57,63,69-75,78] but none of those studies focused on the γ C-terminal helix and apical bearing. The MD strategy devised here explicitly considered the off-axis nature of power strokes, while avoiding heuristic conformational/orientational restraints. In this way, key properties of the γ rotor could be uncovered. Specifically, we were able to provide the mechanistic basis of the experimentally observed H-bond destabilization in the γ C-terminal helix. We found that the torsionally strained γ C-terminal helix is predisposed to stall and unfold, as governed by the interplay of resistive forces in the apical bearing and β-lever power strokes. We envision that once F_1-ATPase is in this locally unfolded state, rotation of γ continues via swivel motions around ϕ/Ψ dihedrals in the kinked segments, analogous to the crosslinked constructs of Hilbers *et al.*[52]

Interestingly, rotation of γ can take place even in F_1 constructs that have a severely truncated γ C-terminal helix (although those conditions result in reduced torque).[79,80] Thus, rotational catalysis is compatible with various scenarios in the apical bearing; these include conditions where the rotor tip is absent,[79,80] immobilized by crosslinking,[52] or transiently unfolded (as seen in this work for wild-type F_1-ATPase).

In a previous HDX-MS investigation[40] we observed destabilization of the γ C-terminal helix in catalytically active F_OF_1, and we also attributed that effect to rotational resistance associated with $\gamma\cdots\alpha_3\beta_3$ contacts in the apical bearing. Interestingly, in F_OF_1 this destabilization of γ was observed only during operation against a PMF-induced counter-torque. The question arises why γ destabilization likewise takes place in F_1-ATPase which does not possess an energized membrane and lacks a PMF-induced

counter-torque. In addition to its apical bearing, the γ rotor in F_OF_1 is secured at its base by the membrane-bound c_{10} ring. Having a bearing at both ends will stabilize the rotation axis of γ (Figure 2.1a). In contrast, F_1-ATPase only possesses a single rotor bearing at the apical end of γ, while the γ foot is unsupported and protrudes into the solvent (Figure 1.1b). The lack of a basal (c_{10}) bearing results in an unstable rotation axis, with bending and lateral movements of γ during power strokes, as seen in Figure 2.4f. Such bending promotes the formation of helix kinks which trigger the disruption of H-bonds (Figure 2.4h, l, p).

This study marks the first time that HDX-MS and steered MD simulations were applied as complementary tools for deciphering the inner workings of a molecular machine, taking advantage of structural insights from X-ray crystallography and cryo-EM. Through further refinement of this combined approach it should be possible to uncover additional details related to rotor operation, power transmission, and mechanochemical energy coupling.

References

1. Walker, J. E. *Biochem. Soc. Trans.* **2013**, *41*, 1-16.
2. Junge, W.; Nelson, N. *Annu. Rev. Biochem.* **2015**, *84*, 631-657.
3. Borsch, M.; Duncan, T. M. *Biochem. Soc. Trans.* **2013**, *41*, 1219-1226.
4. Mitchell, P. *Biochim. Biophys. Acta-Bioenerg.* **2011**, *1807*, 1507-1538.
5. Sielaff, H.; Borsch, M. *Philos. Trans. R. Soc. B-Biol. Sci.* **2013**, *368*.
6. Wachter, A.; Bi, Y. M.; Dunn, S. D.; Cain, B. D.; Sielaff, H.; Wintermann, F.; Engelbrecht, S.; Junge, W. *Proc. Natl. Acad. Sci. U.S.A.* **2011**, *108*, 3924-3929.
7. Hahn, A.; Parey, K.; Bublitz, M.; Mills, D. J.; Zickermann, V.; Vonck, J.; Kuhlbrandt, W.; Meier, T. *Mol. Cell* **2016**, *63*, 445-456.
8. Mazhab-Jafari, M. T.; Rohou, A.; Schmidt, C.; Bueler, S. A.; Benlekbir, S.; Robinson, C. V.; Rubinstein, J. L. *Nature* **2016**, *539*, 118-+.
9. Zhou, A. N.; Rohou, A.; Schep, D. G.; Bason, J. V.; Montgomery, M. G.; Walker, J. E.; Grigorieff, N.; Rubinstein, J. L. *Elife* **2015**, *4*.
10. Shirakihara, Y.; Shiratori, A.; Tanikawa, H.; Nakasako, M.; Yoshida, M.; Suzuki, T. *Febs J.* **2015**, *282*, 2895-2913.
11. Morales-Rios, E.; Montgomery, M. G.; Leslie, A. G. W.; Walker, J. E. *Proc. Natl. Acad. Sci. U.S.A.* **2015**, *112*, 13231-13236.
12. Sobti, M.; Smits, C.; Wong, A. S. W.; Ishmukhametov, R.; Stock, D.; Sandin, S.; Stewart, A. G. *Elife* **2016**, *5*.
13. Cingolani, G.; Duncan, T. M. *Nat. Struct. Mol. Biol.* **2011**, *18*, 701-708.
14. Abrahams, J. P.; Leslie, A. G. W.; Lutter, R.; Walker, J. E. *Nature* **1994**, *370*, 621-628.
15. Mnatsakanyan, N.; Krishnakumar, A. M.; Suzuki, T.; Weber, J. *J. Biol. Chem.* **2009**, *284*, 11336-11345.
16. Martin, J. L.; Ishmukhametov, R.; Hornung, T.; Ahmad, Z.; Frasch, W. D. *Proc. Natl. Acad. Sci. U.S.A.* **2014**, *111*, 3715-3720.
17. Nam, K.; Pu, J. Z.; Karplus, M. *Proc. Natl. Acad. Sci. U.S.A.* **2014**, *111*, 17851-17856.
18. Ishmukhametov, R.; Hornung, T.; Spetzler, D.; Frasch, W. D. *EMBO J.* **2010**, *29*, 3911-3923.
19. Symersky, J.; Pagadala, V.; Osowski, D.; Krah, A.; Meier, T.; Faraldo-Gomez, J. D.; Mueller, D. M. *Nat. Struct. Mol. Biol.* **2012**, *19*, 485-491.
20. Okazaki, K.; Hummer, G. *Proc. Natl. Acad. Sci. U.S.A.* **2015**, *112*, 10720-10725.
21. Czub, J.; Wieczor, M.; Prokopowicz, B.; Grubmuller, H. *J. Am. Chem. Soc.* **2017**, *139*, 4025-4034.

22. Uchihashi, T.; Iino, R.; Ando, T.; Noji, H. *Science* **2011**, *333*, 755-758.

23. Noji, H.; Yasuda, R.; Yoshida, M.; Kinosita, K. *Nature* **1997**, *386*, 299-302.

24. Yasuda, R.; Noji, H.; Kinosita, K.; Yoshida, M. *Cell* **1998**, *93*, 1117-1124.

25. Hirono-Hara, Y.; Noji, H.; Nishiura, M.; Muneyuki, E.; Hara, K. Y.; Yasuda, R.; Kinosita, K.; Yoshida, M. *Proc. Natl. Acad. Sci. U.S.A.* **2001**, *98*, 13649-13654.

26. Adachi, K.; Yasuda, R.; Noji, H.; Itoh, H.; Harada, Y.; Yoshida, M.; Kinosita, K. *Proc. Natl. Acad. Sci. U. S. A.* **2000**, *97*, 7243-7247.

27. Kato-Yamada, Y.; Noji, H.; Yasuda, R.; Kinosita, K.; Yoshida, M. *J. Biol. Chem.* **1998**, *273*, 19375-19377.

28. Pirrone, G. F.; Iacob, R. E.; Engen, J. R. *Anal. Chem.* **2015**, *87*, 99-118.

29. Rand, K. D.; Zehl, M.; Jorgensen, T. J. D. *Acc. Chem. Res.* **2014**, *47*, 3018-3027.

30. Kaltashov, I. A.; Bobst, C. E.; Abzalimov, R. R. *Protein Sci.* **2013**, *22*, 530-544.

31. Chalmers, M. J.; Busby, S. A.; Pascal, B. D.; West, G. M.; Griffin, P. R. *Exp. Rev. Proteomics* **2011**, *8*, 43-59.

32. Percy, A. J.; Rey, M.; Burns, K. M.; Schriemer, D. C. *Anal. Chim. Acta* **2012**, *721*, 7-21.

33. Malhotra, P.; Udgaonkar, J. B. *J. Am. Chem. Soc.* **2016**, *138*, 5866-5878.

34. Zhang, Y.; Rempel, D. L.; Zhang, J.; Sharma, A. K.; Mirica, L. M.; Gross, M. L. *Proc. Natl. Acad. Sci. U.S.A.* **2013**, *110*, 14604-14609.

35. Lee, S.; Wales, T. E.; Escudero, S.; Cohen, D. T.; Luccarelli, J.; Gallagher, C. G.; Cohen, N. A.; Huhn, A. J.; Bird, G. H.; Engen, J. R.; Walensky, L. D. *Nat. Struct. Mol. Biol.* **2016**, *23*, 600-607.

36. Huang, R. Y. C.; Chen, G. D. *Anal. Bioanal. Chem.* **2014**, *406*, 6541-6558.

37. Hvidt, A.; Nielsen, S. O. *Adv. Protein Chem.* **1966**, *21*, 287-386.

38. Englander, S. W.; Mayne, L.; Krishna, M. M. G. *Quart. Rev. Biophys.* **2007**, *40*, 287-326.

39. Cipriano, D. J.; Dunn, S. D. *J. Biol. Chem.* **2002**, *277*, 16782–16790.

40. Vahidi, S.; Bi, Y. M.; Dunn, S. D.; Konermann, L. *Proc. Natl. Acad. Sci. U.S.A.* **2016**, *113*, 2412-2417.

41. Bai, Y.; Milne, J. S.; Mayne, L.; Englander, S. W. *Proteins: Struct., Funct., Genet.* **1993**, *17*, 75-86.

42. Xiao, H.; Hoerner, J. K.; Eyles, S. J.; Dobo, A.; Voigtman, E.; Mel'Cuk, A. I.; Kaltashov, I. A. *Protein Sci.* **2005**, *14*, 543-557.

43. Konermann, L.; Tong, X.; Pan, Y. *J. Mass Spectrom.* **2008**, *43*, 1021-1036.

44. Weis, D. D.; Wales, T. E.; Engen, J. R.; Hotchko, M.; Ten Eyck, L. F. *J. Am. Soc. Mass Spectrom.* **2006**, *17*, 1498-1509.

45. Kapulainen, M.; Ronkainen, H.; Hokkanen, A.; Stuns, I.; Varjus, S.; Nyyssonen, S.; Turunen, R.; Halme, J. *Tribol. Lett.* **2014**, *56*, 47-54.

46. Ueno, H.; Suzuki, T.; Kinosita, K.; Yoshida, M. *Proc. Natl. Acad. Sci. U.S.A.* **2005**, *102*, 1333-1338.

47. Adachi, K.; Oiwa, K.; Nishizaka, T.; Furuike, S.; Noji, H.; Itoh, H.; Yoshida, M.; Kinosita, K. *Cell* **2007**, *130*, 309-321.

48. Czub, J.; Wieczor, M.; Prokopowicz, B.; Grubmuller, H. *J. Am. Chem. Soc.* **2017**, *139*, 4025-4034.

49. Mukherjee, S.; Bora, R. P.; Warshel, A. *Q. Rev. Biophys.* **2015**, *48*, 395-403.

50. Ito, Y.; Ikeguchi, M. *Biophys. J.* **2015**, *108*, 85-97.

51. Bason, J. V.; Montgomery, M. G.; Leslie, A. G. W.; Walker, J. E. *Proc. Natl. Acad. Sci. U. S. A.* **2015**, *112*, 6009-6014.

52. Hilbers, F.; Junge, W.; Sielaff, H. *Plos One* **2013**, *8*.

53. Bowler, M. W.; Montgomery, M. G.; Leslie, A. G. W.; Walker, J. E. *Proc. Natl. Acad. Sci. U.S.A.* **2006**, *103*, 8646-8649.

54. Weber, J.; Wilkemounts, S.; Senior, A. E. *J. Biol. Chem.* **1994**, *269*, 20462-20467.

55. Isralewitz, B.; Gao, M.; Schulten, K. *Curr. Opin. Struct. Biol.* **2001**, *11*, 224-230.

56. Lemkul, J. A.; Bevan, D. R. *J. Phys. Chem. B* **2010**, *114*, 1652-1660.

57. Pu, J.; Karplus, M. *Proc. Natl. Acad. Sci. U.S.A.* **2008**, *105*, 1192-1197.

58. Abrahams, J. P.; Leslie, A. G.; Lutter, R.; Walker, J. E. *Nature* **1994**, *370*, 621--628.

59. Abraham, M. J.; Murtola, T.; Schulz, R.; Páll, S.; Smith, J. C.; Hess, B.; Lindahl, E. *SoftwareX* **2015**, *1–2*, 19-25.

60. Huang, J.; MacKerell, A. D. *J. Comput. Chem.* **2013**, *34*, 2135-2145.

61. Jorgensen, W. L.; Chandrasekhar, J.; Madura, J. D.; Impey, R. W.; Klein, M. L. *J. Chem. Phys.* **1983**, *79*, 926-935.

62. Gibbons, C.; Montgomery, M. G.; Leslie, A. G. W.; Walker, J. E. *Nat. Struct. Biol.* **2000**, *7*, 1055-1061.

63. Okazaki, K.; Hummer, G. *Proc. Natl. Acad. Sci. U.S.A.* **2013**, *110*, 16468-16473.

64. Essmann, U.; Perera, L.; Berkowitz, M. L.; Darden, T.; Lee, H.; Pedersen, L. G. *J. Chem. Phys.* **1995**, *103*, 8577-8593.

65. Bussi, G.; Donadio, D.; Parrinello, M. *J. Chem. Phys.* **2007**, *126*, 0141011-0141017.

66. Parrinello, M.; Rahman, A. *J. Appl. Phys.* **1981**, *52*, 7182-7190.

67. Hoover, W. G. *Phys. Rev. A* **1985**, *31*, 1695-1697.

68. Hess, B.; Kutzner, C.; van der Spoel, D.; Lindahl, E. *J. Chem. Theory Comput.* **2008**, *4*, 435-447.

69. Kutzner, C.; Czub, J.; Grubmuller, H. *J. Chem. Theory Comput.* **2011**, *7*, 1381-1393.

70. Czub, J.; Grubmuller, H. *J. Am. Chem. Soc.* **2014**, *136*, 6960-6968.

71. Dittrich, M.; Hayashi, S.; Schulten, K. *Biophys. J.* **2004**, *87*, 2954-2967.

72. Mukherjee, S.; Warshel, A. *Proc. Natl. Acad. Sci. U.S.A.* **2011**, *108*, 20550-20555.

73. Mukherjee, S.; Warshel, A. *Proc. Natl. Acad. Sci. U.S.A.* **2015**, *112*, 2746-2751.

74. Koga, N.; Takada, S. *Proc. Natl. Acad. Sci. U.S.A.* **2006**, *103*, 5367-5372.

75. Czub, J.; Grubmuller, H. *Proc. Natl. Acad. Sci. U.S.A.* **2011**, *108*, 7408-7413.

76. Junge, W.; Sielaff, H.; Engelbrecht, S. *Nature* **2009**, *459*, 364-370.

77. Torshin, I. Y.; Weber, I. T.; Harrison, R. W. *Protein Eng.* **2002**, *15*, 359-363.

78. Isaka, Y.; Ekimoto, T.; Kokabu, Y.; Yamato, I.; Murata, T.; Ikeguchi, M. *Biophys. J.* **2017**, *112*, 911-920.

79. Hossain, M. D.; Furuike, S.; Maki, Y.; Adachi, K.; Suzuki, T.; Kohori, A.; Itoh, H.; Yoshida, M.; Kinosita, K. *Biophys. J.* **2008**, *95*, 4837-4844.

80. Furuike, S.; Hossain, M. D.; Maki, Y.; Adachi, K.; Suzuki, T.; Kohori, A.; Itoh, H.; Yoshida, M.; Kinosita, K. *Science* **2008**, *319*, 955-958.

3 Conclusions and Future Work

3.1 Conclusions

Experiments and MD simulations have played an important role in efforts to decipher the F_OF_1 rotary mechanisms.[1-14] Yet we are still far from understanding the complete mechanism of this molecular motor. Steered MD protocols and related modeling approaches have previously been applied to ATPases,[12,15-27] but none of those studies focused on the γ C-terminal helix and apical bearing. In this work, we devised an MD strategy that considered the off-axis nature of power strokes, while avoiding heuristic conformational/orientational restraints. When F_1-ATPase was subjected to the off-axis force rotation scheme developed here, we were able to identify significant contacts between γ and $\alpha_3\beta_3$ in the apical bearing that lead to destabilization/unfolding in the γ C-terminal helix, consistent with the HDX experimental data from our own laboratory.[28] This leads us to believe that once F_1-ATPase is in this locally unfolded state, rotation of γ can continue via swivel motions around ϕ/Ψ dihedrals in the kinked segments, similar to the crosslinked constructs of Hilbers *et al.*[29]

There are still many difficulties in studying a large protein complex, such as ATPase. One of the major factors that complicates the simulation of ATPase is simulation time itself. We believe the rotation speed of these types of simulations play an important role in determining the proper mechanism of γ rotation. In this work we were able to decrease the rotation rate to 3.3° ns^{-1}, which is still fast compared to experimental

rotation rates of ~3×10^{-4} ° ns^{-1}.[14] If slower rotation rates were possible, we believe that more sidechain conformations between γ and the apical bearing would be sampled allowing the strained y helix to "glide" during rotation. Yet, such endeavours are very challenging with currently available computational resources. Despite the difference in time scale, it is remarkable how well the MD-predicted H-bond opening events agree with the experimentally detected HDX hot spot in the γ C-terminal helix. This leads us to believe that this region is more flexible than might be expected from X-ray structural data where this helix was considered to be part of a more or less rigid rotor.[30]

3.2 Future Work – Off-Axis Force Rotation Studies of F_OF_1

In Figure 1.6, Vahidi *et al.* observed destabilization of the γ C-terminal helix in catalytically active F_OF_1.[31] This destabilization was attributed to rotational resistance associated with γ···$\alpha_3\beta_3$ contacts in the apical bearing. The destabilization of γ was observed only during operation against a PMF-induced counter-torque. The question arises why γ destabilization likewise takes place in F_1-ATPase which does not possess an energized membrane and lacks a PMF-induced counter-torque. The reason for this destabilization in the F_1-ATPase system was linked to the lack of a basal (c_{10}) bearing resulting in an unstable rotation axis. What remains uncertain is how at a molecular level, a PMF-induced counter-torque promotes the destabilization of the γ C-terminal helix in F_OF_1 with a stable rotation axis.

Through further refinement of our Steered MD and HDX-MS combined approach it should be possible to uncover additional details related to rotor operation, power transmission, and mechanochemical energy coupling in intact F_OF_1. For example, we

believe that our off-axis force rotation can shed light onto the F_OF_1 γ C-terminal helix destabilization under PMF-induced counter-torquer. The best way to approach this problem would be to model F_OF_1 ATP synthase by restraining γ on a stable rotational axis to mimic the presence of the c_n ring. This would allow us to save computational power by only using the F_1 domain of the system, which would reduce the number of atoms in the simulation. From here, a proper counter-torque method would need to be established to be applied to our off-axis force rotation. By comparing both counter-torque and non-counter-torque simulations we believe that it should be possible to decipher reasons for γ destabilization under counter-torque conditions. This will bring us closer to discovering further reasons to the flexibility of the γ subunit and how this unexpected mechanical feature of the ATP synthase motor is consistent with high efficiency catalysis.

References

1. Walker, J. E. *Biochem. Soc. Trans.* **2013**, *41*, 1-16.
2. Sielaff, H.; Borsch, M. *Philos. Trans. R. Soc. B-Biol. Sci.* **2013**, *368*.
3. Wachter, A.; Bi, Y. M.; Dunn, S. D.; Cain, B. D.; Sielaff, H.; Wintermann, F.; Engelbrecht, S.; Junge, W. *Proc. Natl. Acad. Sci. U.S.A.* **2011**, *108*, 3924-3929.
4. Junge, W.; Nelson, N. *Annu. Rev. Biochem.* **2015**, *84*, 631-657.
5. Hahn, A.; Parey, K.; Bublitz, M.; Mills, D. J.; Zickermann, V.; Vonck, J.; Kuhlbrandt, W.; Meier, T. *Mol. Cell* **2016**, *63*, 445-456.
6. Mazhab-Jafari, M. T.; Rohou, A.; Schmidt, C.; Bueler, S. A.; Benlekbir, S.; Robinson, C. V.; Rubinstein, J. L. *Nature* **2016**, *539*, 118-+.
7. Zhou, A. N.; Rohou, A.; Schep, D. G.; Bason, J. V.; Montgomery, M. G.; Walker, J. E.; Grigorieff, N.; Rubinstein, J. L. *Elife* **2015**, *4*.
8. Shirakihara, Y.; Shiratori, A.; Tanikawa, H.; Nakasako, M.; Yoshida, M.; Suzuki, T. *Febs J.* **2015**, *282*, 2895-2913.
9. Morales-Rios, E.; Montgomery, M. G.; Leslie, A. G. W.; Walker, J. E. *Proc. Natl. Acad. Sci. U.S.A.* **2015**, *112*, 13231-13236.
10. Sobti, M.; Smits, C.; Wong, A. S. W.; Ishmukhametov, R.; Stock, D.; Sandin, S.; Stewart, A. G. *Elife* **2016**, *5*.
11. Cingolani, G.; Duncan, T. M. *Nat. Struct. Mol. Biol.* **2011**, *18*, 701-708.
12. Okazaki, K.; Hummer, G. *Proc. Natl. Acad. Sci. U.S.A.* **2015**, *112*, 10720-10725.
13. Czub, J.; Wieczor, M.; Prokopowicz, B.; Grubmuller, H. *J. Am. Chem. Soc.* **2017**, *139*, 4025-4034.
14. Martin, J. L.; Ishmukhametov, R.; Hornung, T.; Ahmad, Z.; Frasch, W. D. *Proc. Natl. Acad. Sci. U.S.A.* **2014**, *111*, 3715-3720.
15. Dittrich, M.; Hayashi, S.; Schulten, K. *Biophys. J.* **2004**, *87*, 2954-2967.
16. Mukherjee, S.; Warshel, A. *Proc. Natl. Acad. Sci. U.S.A.* **2011**, *108*, 20550-20555.
17. Mukherjee, S.; Bora, R. P.; Warshel, A. *Q. Rev. Biophys.* **2015**, *48*, 395-403.
18. Mukherjee, S.; Warshel, A. *Proc. Natl. Acad. Sci. U.S.A.* **2015**, *112*, 2746-2751.
19. Koga, N.; Takada, S. *Proc. Natl. Acad. Sci. U.S.A.* **2006**, *103*, 5367-5372.
20. Pu, J.; Karplus, M. *Proc. Natl. Acad. Sci. U.S.A.* **2008**, *105*, 1192-1197.
21. Nam, K.; Pu, J. Z.; Karplus, M. *Proc. Natl. Acad. Sci. U.S.A.* **2014**, *111*, 17851-17856.
22. Czub, J.; Wieczor, M.; Prokopowicz, B.; Grubmuller, H. *J. Am. Chem. Soc.* **2017**, *139*, 4025-4034.

23. Czub, J.; Grubmuller, H. *Proc. Natl. Acad. Sci. U.S.A.* **2011**, *108*, 7408-7413.

24. Czub, J.; Grubmuller, H. *J. Am. Chem. Soc.* **2014**, *136*, 6960-6968.

25. Kutzner, C.; Czub, J.; Grubmuller, H. *J. Chem. Theory Comput.* **2011**, *7*, 1381-1393.

26. Okazaki, K.; Hummer, G. *Proc. Natl. Acad. Sci. U.S.A.* **2013**, *110*, 16468-16473.

27. Isaka, Y.; Ekimoto, T.; Kokabu, Y.; Yamato, I.; Murata, T.; Ikeguchi, M. *Biophys. J.* **2017**, *112*, 911-920.

28. Murcia Rios, A.; Vahidi, S.; Dunn, S. D.; Konermann, L. *J. Am. Chem. Soc.* **2018**, *140*, 14860-14869.

29. Hilbers, F.; Junge, W.; Sielaff, H. *Plos One* **2013**, *8*.

30. Abrahams, J. P.; Leslie, A. G. W.; Lutter, R.; Walker, J. E. *Nature* **1994**, *370*, 621-628.

31. Vahidi, S.; Bi, Y. M.; Dunn, S. D.; Konermann, L. *Proc. Natl. Acad. Sci. U.S.A.* **2016**, *113*, 2412-2417.

Appendix I – Permissions

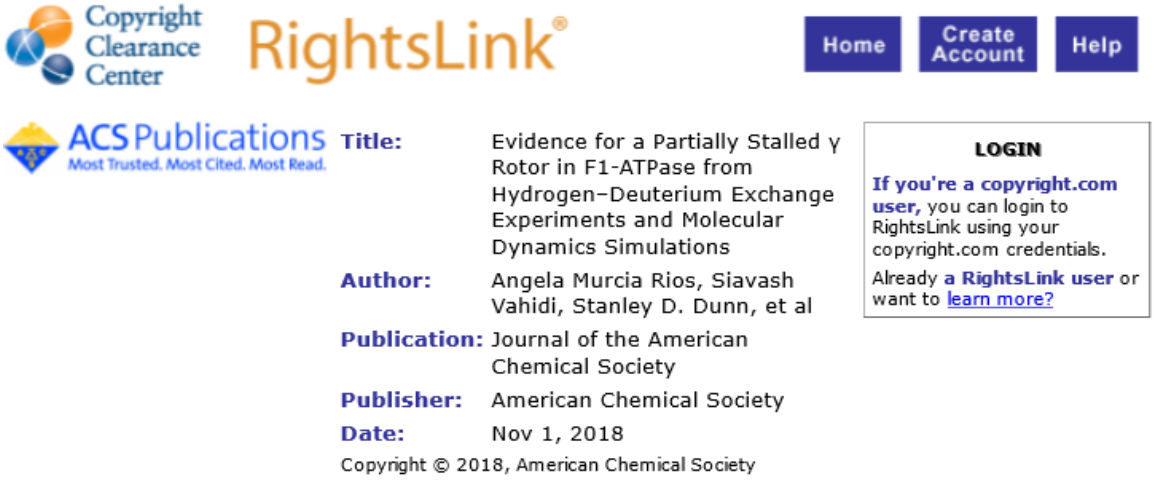

Copyright Clearance Center RightsLink®

Home | Create Account | Help

ACS Publications
Most Trusted. Most Cited. Most Read.

Title: Evidence for a Partially Stalled γ Rotor in F1-ATPase from Hydrogen–Deuterium Exchange Experiments and Molecular Dynamics Simulations

Author: Angela Murcia Rios, Siavash Vahidi, Stanley D. Dunn, et al

Publication: Journal of the American Chemical Society

Publisher: American Chemical Society

Date: Nov 1, 2018

Copyright © 2018, American Chemical Society

LOGIN

If you're a copyright.com user, you can login to RightsLink using your copyright.com credentials.

Already **a RightsLink user** or want to learn more?

PERMISSION/LICENSE IS GRANTED FOR YOUR ORDER AT NO CHARGE

This type of permission/license, instead of the standard Terms & Conditions, is sent to you because no fee is being charged for your order. Please note the following:

- Permission is granted for your request in both print and electronic formats, and translations.
- If figures and/or tables were requested, they may be adapted or used in part.
- Please print this page for your records and send a copy of it to your publisher/graduate school.
- Appropriate credit for the requested material should be given as follows: "Reprinted (adapted) with permission from (COMPLETE REFERENCE CITATION). Copyright (YEAR) American Chemical Society." Insert appropriate information in place of the capitalized words.
- One-time permission is granted only for the use specified in your request. No additional uses are granted (such as derivative works or other editions). For any other uses, please submit a new request.

BACK | CLOSE WINDOW

Rights and Permissions

← About

The author(s) retains copyright to individual PNAS articles, and the National Academy of Sciences of the United States of America (NAS) holds copyright to the collective work and retains an exclusive License to Publish these articles, except for open access articles submitted beginning September 2017. For such open access articles, NAS retains a nonexclusive License to Publish, and these articles are distributed under either a CC BY-NC-ND or CC BY license.

For volumes 106–114 (2009–September 2017), the author(s) retains copyright to individual articles, and NAS retains an exclusive License to Publish these articles and holds copyright to the collective work. Volumes 90–105 (1993–2008) are copyright National Academy of Sciences. For volumes 1–89 (1915–1992), the author(s) retains copyright to individual articles, and NAS holds copyright to the collective work.

Authors whose work will be reused should be notified. Use of PNAS material must not imply any endorsement by PNAS or NAS. The full journal reference must be cited and, for articles published in Volumes 90–105 (1993–2008), "Copyright (copyright year) National Academy of Sciences."

Please visit the Permissions FAQ for detailed information about PNAS copyright and self-archiving guidelines. The PNAS listing on the Sherpa RoMEO publisher policies pages can be found here.

Additional information and answers to frequently asked questions about author rights and permissions are available on our FAQ page.

Requesting Permission

Anyone may, without requesting permission, use original figures or tables published in PNAS for noncommercial and educational use (i.e., in a review article, in a book that is not for sale), provided that the full journal reference is cited and, for articles published in volumes 90–105 (1993–2008), "Copyright (copyright year) National Academy of Sciences." Commercial reuse of figures and tables (i.e., in promotional materials, in a textbook for sale) requires permission from PNAS.

Text and data mining are permitted for noncommercial institutions with an active institutional site license to PNAS for internal noncommercial research purposes. Other requests should be sent to PNASpermissions@nas.edu.

Curriculum Vitae

Name: Angela Marcela Murcia Rios

Post-secondary Education and Degrees:

M.Sc. in Chemistry (2017-present)
The University of Western Ontario
London, Ontario, Canada
Supervisor: Prof. Lars Konermann

Honors B.Sc. in Chemistry (2012-2017)
The University of Western Ontario
London, Ontario, Canada
Supervisor: Prof. Lars Konermann

Related Work Experience

Graduate Teaching Assistant
The University of Western Ontario
- Organic Chemistry for Life Sciences (Fall 2017, 2018)
- Microscopic Phenomena (Winter 2018, 2019)

Summer Research Assistant (2015, 2016)
The University of Western Ontario
Supervisor: Prof. Viktor N. Staroverov

Honours and Awards:

Lipson-Baines Graduate Departmental Seminar Award
The University of Western Ontario (2019)

Best Oral Presentation Award, 2nd Place
45th SOUSCC (2017)

Dean's Honor List, Faculty of Science
The University of Western Ontario (2016, 2017)

Western Scholarship of Distinction
The University of Western Ontario (2012)

Highland Pharmacy Award
(in support of studies at UWO)
London District Catholic School Board (2012)

Student Council Award for Math and Business
(in support of studies at UWO)
London District Catholic School Board (2012)

Publications:

A. M. Murcia Rios, S. Vahidi, S. D. Dunn, and L. Konermann. Evidence for a Partially Stalled γ Rotor in F_1-ATPase from H/D Exchange Experiments and Molecular Dynamics Simulations. *J. Am. Chem. Soc.* **2018**, *140*, 14860.

A. M. Murcia Rios, D. N. Komsa, and V. N. Staroverov. Effects of Dispersion Corrections and Nonlocality on Density-Functional Predictions of Pressure-Induced Polymorphic Transitions of Crystalline Diborane. *J. Phys. Chem. C* **2018**, *122*, 14781.

Conference Presentations:

A. M. Murcia Rios, and L. Konermann "Investigating the Rotary Mechanism of F_1-ATPase Using Molecular Dynamics Simulations" (poster), *101st Canadian Chemistry Conference and Exhibition*, **May 27−31, 2018**, Edmonton, AB, Canada.

A. M. Murcia Rios, and L. Konermann "Investigating the Rotary Mechanism of ATPase Using Molecular Dynamics Simulations" (oral), *45th Southern Ontario Undergraduate Student Chemistry Conference*, **March 18, 2017**, Toronto, ON, Canada.